

Diagnosing symplecticity in simulations of high-dimensional Hamiltonian systems

William Barham¹ and J. W. Burby²

¹Los Alamos National Laboratory, Theoretical Division

²The University of Texas at Austin, Institute for Fusion Studies and Department of Physics

December 17, 2025

Abstract

Integrals of the Liouville 1-form, known as the first Poincaré integral invariant, provide a computable figure of merit for monitoring the conservation of symplecticity in the numerical integration of Hamiltonian systems. These integrals may be approximated with spectral convergence in the number of sample points, limited only by the regularity of the Hamiltonian. We devise a numerical integral invariant diagnostic for checking preservation of symplecticity in particle-in-cell (PIC) kinetic plasma simulation codes. As a first application of this diagnostic tool, we check the preservation of symplecticity in symplectic electrostatic particle-in-cell (PIC) methods. Surprisingly, such PIC methods fail to have symplectic time-advance maps if the charge is interpolated to the grid using linear shape functions, as is commonly done in practice. It is found that at least quadratic interpolation is needed for a structure-preserving PIC method to truly be symplectic.

Contents

1	Introduction	2
2	Mathematical preliminaries	3
2.1	Hamiltonian systems and symplecticity	3
2.2	A conserved loop integral	4
2.3	Approximating the loop integral	5
2.4	Convergence of the the loop integral approximations	6
2.5	Approximating the loop integral as a function of time	7
3	A computable diagnostic for symplecticity	8
3.1	A diagnostic for symplecticity	8
3.2	Illustrative example: the shearing of phase-space loops	9
3.3	Conservative, nearly-symplectic systems	10

4 On the symplecticity of low regularity Hamiltonian systems	11
4.1 Interpretation of flow maps for low-regularity Hamiltonian systems	11
4.2 Hamiltonian splitting flow maps for piecewise linear potentials	12
4.3 Example: an interpolated nonlinear pendulum	14
4.4 Example: a nonlinear pendulum array	16
4.5 Discussion	18
5 Symplectic electrostatic particle-in-cell methods	19
5.1 Symplectic PIC methods	19
5.2 Applying the symplectic diagnostic to PIC	20
5.3 The effects of smoothing in PIC methods	21
6 Conclusion	26
A The convergence rate of the high-regularity loop integral approximation	30
A.1 The pseudospectral loop integral approximation	31
B The convergence rate of the low-regularity loop integral approximation	35
B.1 The piecewise loop integral and its approximation	36
B.2 Detecting jump discontinuities	38
C On the regularity of B-splines in 1D	38
D On the symplecticity of Strang splitting	39
E Two-cell, single-particle linear PIC evolution equations	41

1 Introduction

Symplectic integrators are a natural and popular method for the numerical integration of Hamiltonian ordinary differential equations. In addition to simulating Hamiltonian ordinary differential equations [27], they are frequently used for the temporal integration of wave-like partial differential equations (e.g. symplectic Runge-Kutta methods [50] or splitting methods [39]), and are commonly used in time-stepping schemes for structure-preserving particle-in-cell (PIC) kinetic plasma simulation methods [53, 47, 38, 45, 56, 19, 29, 7, 22, 23, 46, 35, 51, 54, 47, 34, 33]. Likewise, symplectic integration has been used to time-advance the Vlasov equation when coupled with spatial discretizations other than particle-in-cell, although the semi-discrete system is not Hamiltonian in such cases [2, 8]. Symplectic integrators are designed such that the time-advance map is a canonical transformation, thus conserving a symplectic form exactly. A consequence of this defining property of symplectic integrators is the conservation of a numerical energy which remains close to the true energy for the duration of the simulation. This energy stability property is frequently cited as a justification for the use of symplectic integrators. However, there are non-symplectic, energy-conserving integrators, somewhat dulling this argument for their utility [14, 13, 12, 15, 11, 10, 49, 36, 32]. A better justification for the value of symplectic integration is the exact conservation of the symplectic form. This more fundamental property of symplectic integrators, while a clear theoretical advantage, is difficult to directly quantify in a simulation, and is sometimes overlooked in practice due to its abstractness and the difficulty of measuring its impact.

This work proposes a diagnostic tool based on the Poincaré integral invariant which directly measures the conservation of the symplectic form. This integral invariant was previously used to monitor

symplecticity conservation in variational integrators and related schemes for low-dimensional degenerate Lagrangian systems [37]. In this work, the suitability of such a diagnostic for monitoring the symplecticity of PIC methods is a central concern, with challenges such as high-dimensionality and low-regularity being addressed in detail. Notably, we are forced to address two issues associated with integral invariants absent from previous work [37] in low dimensions. (1) Chaos reigns in high dimensions, leading to generic and rapid shearing of the phase space loops around which the Liouville 1-form is integrated. (2) The time advance map for a discretized PDE system generally only enjoys limited regularity, and therefore does not fall under the purview of the most elementary results establishing integral invariance. Our work provides a general purpose tool to aid in software-development and in analyzing the relative performance of symplectic and non-symplectic time-stepping methods.

2 Mathematical preliminaries

This section briefly introduces some essential background knowledge of Hamiltonian systems.

2.1 Hamiltonian systems and symplecticity

The diagnostic tool of interest in this work is applicable to numerical approximations of Hamiltonian systems. Given a state vector $\mathbf{z} = (\mathbf{q}, \mathbf{p}) \in \mathbb{R}^{2d}$, where $\mathbf{q}, \mathbf{p} \in \mathbb{R}^d$, and a Hamiltonian, $\mathcal{H} : \mathbb{R}^{2d} \rightarrow \mathbb{R}$, a canonical Hamiltonian system evolves as

$$\dot{\mathbf{z}} = J_c \nabla \mathcal{H}, \quad J_c = \begin{pmatrix} 0 & I_d \\ -I_d & 0 \end{pmatrix}, \quad (1)$$

where $I_d \in \mathbb{R}^{d \times d}$ is the identity matrix. The matrix J_c is variously called the canonical Poisson tensor, the Hamiltonian bivector, or the Poisson matrix. Its inverse is the canonical symplectic form, $\omega_c = d\mathbf{q} \wedge d\mathbf{p} = \sum_{i=1}^d dq_i \wedge dp^i$. In more common notation, we write

$$\dot{\mathbf{q}} = \frac{\partial \mathcal{H}}{\partial \mathbf{p}}, \quad \text{and} \quad \dot{\mathbf{p}} = -\frac{\partial \mathcal{H}}{\partial \mathbf{q}}. \quad (2)$$

Such systems, and their complimentary Lagrangian formulation, are the central object of study in classical mechanics.

Systems of this form conserve energy and symplecticity. Let the time-advance map for solutions of equation (1) be denoted by $\Phi_h : \mathbf{z}(t) \mapsto \mathbf{z}(t+h)$, and let $D_{\mathbf{z}} \Phi_h$ denote its Jacobian. Then these two conservation laws may be expressed as follows:

- *Energy is conserved:* $\mathcal{H}(\mathbf{z}(t)) = \text{const.}$
- *The time-advance map is symplectic:* $D_{\mathbf{z}} \Phi_h^T J_c D_{\mathbf{z}} \Phi_h = J_c, \forall t.$

The former is a direct consequence of the anti-symmetry of the Poisson matrix, while the conservation of symplecticity is a deeper result associated with the geometry of phase-space.

A symplectic integrator is a computable approximation to the time-advance map, $\tilde{\Phi}_h \approx \Phi_h$, such that $D_{\mathbf{z}} \tilde{\Phi}_h^T J_c D_{\mathbf{z}} \tilde{\Phi}_h = J_c$. One may show [27] that if \mathcal{H} is real analytic then energy is nearly conserved over exponentially long time intervals by a symplectic integrator:

$$|\mathcal{H}(\tilde{\Phi}_h^n \mathbf{z}_0) - \mathcal{H}(\mathbf{z}_0)| = O(h^p) + O(n h e^{-\gamma/(\omega h)}) \quad \forall n \geq 0, \quad (3)$$

where p is the order of discretization error, γ depends on the method, and ω is related to the Lipschitz constant of the vector field. That is, the energy computed oscillates around a mean value in a band of width $O(h^p)$.

While energy conservation is quite simple to verify, reliably monitoring the conservation of symplecticity in a simulation is difficult. The ease of monitoring energy conservation follows from the energy conservation law's dependence on individual trajectories. In contrast, symplecticity pertains to the organization of trajectories in phase space space; there is no simple method for checking symplecticity preservation along an individual trajectory without knowledge of nearby trajectories. As we will see, probing symplecticity conservation can be accomplished using parameterized families of trajectories. Despite this additional challenge in monitoring the conservation of symplecticity, the endeavor is worthwhile, as energy conservation is not an ideal figure of merit to monitor symplecticity. Symplectic integrators do not identically conserve energy, and many non-symplectic methods conserve energy exactly, both in the context of PIC [14, 13, 12, 15, 11, 10, 49, 36, 32], or for general Hamiltonian systems using discrete gradients and related methods [24, 41, 48, 9, 26].

2.2 A conserved loop integral

To introduce a more appropriate figure of merit to monitor symplecticity, it is necessary to briefly establish some notation and terminology. The *Liouville 1-form* is $\vartheta = \mathbf{p} \cdot \mathbf{d}\mathbf{q} = \sum_{i=1}^d p_i \mathbf{d}q^i$. Minus the exterior derivative of the Liouville 1-form is the canonical symplectic form: $\omega_c = -\mathbf{d}\vartheta$. For a given Hamiltonian, \mathcal{H} , we denote the corresponding Hamiltonian vector field by \mathbf{X}_H . The Hamiltonian vector field is determined by \mathcal{H} and ω_c according to

$$\iota_{\mathbf{X}_H} \omega_c = \mathbf{d}\mathcal{H}, \quad (4)$$

or, equivalently, $\mathbf{X}_H = J_c \nabla \mathcal{H}$, since this work considers the state space \mathbb{R}^{2d} with its standard inner product. When it exists, the *flow map* for \mathbf{X}_H , $\Phi_t^{\mathcal{H}} : \mathbb{R}^{2d} \rightarrow \mathbb{R}^{2d}$, is the unique t -dependent mapping such that

$$\forall \mathbf{z}_0 \in \mathbb{R}^{2d}, \quad \frac{d}{dt} \Phi_t^{\mathcal{H}}(\mathbf{z}_0) = \mathbf{X}_H(\Phi_t^{\mathcal{H}}(\mathbf{z}_0)) \text{ and } \Phi_0^{\mathcal{H}}(\mathbf{z}_0) = \mathbf{z}_0. \quad (5)$$

It is well-known that ω_c is conserved by a Hamiltonian flow:

$$\frac{d}{dt} (\Phi_t^{\mathcal{H}})^* \omega_c = (\Phi_t^{\mathcal{H}})^* (\mathcal{L}_{\mathbf{X}_H} \omega_c) = (\Phi_t^{\mathcal{H}})^* (\mathbf{d}\iota_{\mathbf{X}_H} \omega_c + \iota_{\mathbf{X}_H} \mathbf{d}\omega_c) = (\Phi_t^{\mathcal{H}})^* (\mathbf{d}^2 \mathcal{H} + 0) = 0, \quad (6)$$

where the first equality follows from the definition of the Lie derivative, the second from Cartan's formula, the third from equation (4) and the fact that ω_c is closed, and finally the last equality follows from the fact that $\mathbf{d}^2 = 0$. Note, this result is equivalent to the previously stated criterion for the time-advance map being symplectic, since $J_c^{-1} = \omega_c$.

For any oriented 2-dimensional submanifold $D \subset \mathbb{R}^{2d}$, we have that

$$\int_{\Phi_t^{\mathcal{H}}(D)} \omega_c = \int_D (\Phi_t^{\mathcal{H}})^* \omega_c = \int_D \omega_c. \quad (7)$$

In particular, if $\partial D = \gamma$ such that $\gamma : \mathbb{R} \text{ mod } 1 \rightarrow \mathbb{R}^{2d} : \theta \mapsto (\gamma^x(\theta), \gamma^p(\theta))$ is a parameterized loop in phase-space, one may use Stokes' theorem to deduce a second conserved integral:

$$\mathcal{I}(t) = \int_{\Phi_t^{\mathcal{H}} \circ \gamma} \vartheta = \int_{\gamma} \vartheta. \quad (8)$$

This follows because Stokes' theorem implies

$$\int_{\Phi_t^{\mathcal{H}} \circ \gamma} \vartheta = \int_{\partial \Phi_t^{\mathcal{H}}(D)} \vartheta = - \int_{\Phi_t^{\mathcal{H}}(D)} \omega_c = - \int_D \omega_c = \int_{\gamma} \vartheta, \quad (9)$$

as long as $\partial \Phi_s^{\mathcal{H}}(D) = \gamma \circ \Phi_s^{\mathcal{H}}$. This is ensured if the map $\Phi_s^{\mathcal{H}}$ is a bijective C^0 map. The loop integral $\mathcal{I}(t)$ defined in equation (8) is known as the (first) *Poincaré integral invariant*. This quantity is the basis for the numerical diagnostic tool considered in this work.

2.3 Approximating the loop integral

An arbitrary loop γ in phase space cannot generally be computed analytically. Hence, we must approximate the integral $\int_{\gamma} \vartheta$. We wish to make this approximation only having access to a finite number of samples of a parameterized loop. That is, given $\gamma : \mathbb{R} \bmod 1 \rightarrow \mathbb{R}^{2d}$, we have access to the data:

$$\gamma(k\Delta s) = (\mathbf{q}_{k+1}, \mathbf{p}_{k+1}) \in \mathbb{R}^d \times \mathbb{R}^d, \quad \text{for } k \in \{0, 1, 2, \dots, N_s - 1\}, \quad (10)$$

where $\Delta s = 1/N_s$. As a matter of notation, we collect the loop-data in a matrix: $\mathbf{q}, \mathbf{p} \in \mathbb{R}^{N_s \times d}$, such that

$$\mathbf{q} = \begin{bmatrix} \mathbf{q}_1^T \\ \mathbf{q}_2^T \\ \vdots \\ \mathbf{q}_{N_s}^T \end{bmatrix}, \quad \text{and} \quad \mathbf{p} = \begin{bmatrix} \mathbf{p}_1^T \\ \mathbf{p}_2^T \\ \vdots \\ \mathbf{p}_{N_s}^T \end{bmatrix}. \quad (11)$$

This organization of the data makes it convenient to apply linear operators in loop space as matrices. In particular, the derivative in loop space is applied as a matrix. We have considered two different approximations of the loop integral whose convergence rate depends on the regularity of the loop data: a Fourier-pseudospectral approximation and a finite difference approximation. The proofs of convergence for these two methods are given in Appendix A and Appendix B, respectively.

Pseudospectral approximation: If \mathbb{F} is the discrete Fourier transform matrix, and $\text{diag}(\mathbf{k})$ is the diagonal matrix with the appropriately selected wavenumbers to apply the derivative in Fourier space, then the pseudospectral approximation to the derivative in loop space is given by

$$\mathbb{D}\mathbf{q} = \mathbb{F}^{-1} (i \text{diag}(\mathbf{k}) \mathbb{F}\mathbf{q}). \quad (12)$$

To be absolutely clear, $(\mathbb{D}\mathbf{q})_{ij} = \sum_{k=1}^{N_s} \mathbb{D}_{ik} \mathbf{q}_{kj}$. This approximation of the derivative is spectrally convergent for smooth periodic functions. Using trapezoidal rule, which is likewise spectrally convergent for smooth periodic functions, the loop integral may be approximated as follows:

$$\mathcal{I} = \oint_{\gamma} \mathbf{p} \cdot d\mathbf{q} = \int_0^1 \mathbf{p}(s) \cdot \frac{\partial \mathbf{q}}{\partial s} ds \approx \mathbf{p} : (\mathbb{D}\mathbf{q}) \Delta s = \sum_{i=1}^d \sum_{j,k=1}^{N_s} \mathbf{p}_{ki} \mathbb{D}_{kj} \mathbf{q}_{ji} \Delta s =: \mathcal{I}_N, \quad (13)$$

where the colon notation contracts two matrices: for $A, B \in \mathbb{R}^{n \times m}$, $A : B = \sum_{i,j=1}^{n,m} A_{ij} B_{ij}$.

Remark 1. *As a technical note, if (\mathbf{q}, \mathbf{p}) represents the state of a discretized Hamiltonian PDE system with periodic boundary conditions it is necessary to unwrap the data prior to computing the pseudospectral loop integral approximation to eliminate jumps at the edges of the spatial domain.*

Finite difference approximation: The finite difference approximation is defined as

$$\mathcal{I}_N := \sum_{i=1}^d \sum_{k \in \mathcal{K}_i(L_q, L_p)} \mathbf{p}_{ik} (\mathbf{q}_{i,k+1} - \mathbf{q}_{ik}), \quad (14)$$

where

$$\mathcal{K}_i(L_q, L_p) = \left\{ k \in \{0, \dots, N-1\} : \left| \frac{\mathbf{p}_{i,k+1} - \mathbf{p}_{ik}}{\Delta s} \right| \leq L_p \|p\|_{L^\infty([0,1])} \right. \\ \left. \text{and} \quad \left| \frac{\mathbf{q}_{i,k+1} - \mathbf{q}_{ik}}{\Delta s} \right| \leq L_q \|q\|_{L^\infty([0,1])} \right\}. \quad (15)$$

This approximation uses a forward difference to approximate $q'(s)$ and approximates the integral as a Riemann sum, while omitting sub-intervals where the derivative of q or p exceeds a user-specified threshold given by the parameters L_q and L_p .

Remark 2. *This approximation converges quite slowly, see appendix B. Therefore, the finite difference approximation should only be used in cases where the pseudospectral approximation fails to converge, e.g. loops with discontinuities.*

Remark 3. *To our knowledge, there is no complete theory for the conservation of the Poincaré integral invariant by Hamiltonian flows with insufficient regularity to guarantee the spatial continuity of the flow map, e.g. systems with discontinuous Hamiltonian vector fields. Indeed, the classical existence and uniqueness theory for ODEs assumes Lipschitz vector fields [28], and, for systems with less regularity, one must resort to a weaker interpretation of the solution map [1]. Despite these difficulties, we consider an approximation of the loop integral which remains defined even for discontinuous data for reasons discussed in Section 4.2.*

2.4 Convergence of the the loop integral approximations

In appendix A, we show that the error in a pseudospectral approximation based on N data points scales like $O(N^{-(2r-1)})$, when $q, p \in H_{per}^r([0, 1])$, for $r > 1/2$. In appendix B, we show that the error in a simple finite difference approximation of the loop integral scales like $O(N^{-1})$ for piecewise smooth q, p with a finite number of discontinuities.

In these appendices, we demonstrate the convergence of approximations to loop integrals of the form

$$\mathcal{I}(p, q) = \int_0^1 p(s) dq(s) = \int_0^1 p(s) q'(s) ds. \quad (16)$$

However, we may consider higher-dimensional phase spaces simply by adding up individual one-dimensional loops:

$$\mathcal{I}(\mathbf{p}, \mathbf{q}) = \int_{\gamma} \mathbf{p} \cdot d\mathbf{q} = \int_0^1 \mathbf{p}(s) \cdot \frac{d\mathbf{q}}{ds} ds = \sum_{i=1}^d \int_0^1 p_i(s) \frac{dq^i}{ds} ds. \quad (17)$$

The triangle inequality allows us to reduce the convergence analysis of approximations to loop integrals in higher dimensional phase-space to the original scalar case. This is because both the continuous and approximate loop integrals split additively over each degree of freedom. Hence, we find that the pseudospectral approximation of the loop integral in \mathbb{R}^{2d} for H^r data scales as

$$|\mathcal{I}(\mathbf{p}, \mathbf{q}) - \mathcal{I}_N(\mathbf{p}, \mathbf{q})| = O(dN^{-(2r-1)}), \quad (18)$$

while the finite difference approximation scales as

$$|\mathcal{I}(\mathbf{p}, \mathbf{q}) - \mathcal{I}_N(\mathbf{p}, \mathbf{q})| = O(dN^{-1}). \quad (19)$$

For high-dimensional systems with low regularity, a large number of sample points may be needed.

The pseudospectral approximation makes an intermediate approximation through a Fourier-Galerkin approximation to the loop integral. The error bound on this approximation is very likely sharp (although not proven so). For high-regularity loop data, we do not anticipate any other approximation based on equispaced loop samples to converge faster than the Fourier-collocation approach. In the low-regularity case, the finite difference approximation of the loop integral converges slowly. However, we do not anticipate there being superior approximations based solely on data on an equispaced grid. Quadrature rules for integrals of discontinuous data with high-order convergence require a priori knowledge of the location of the discontinuities (e.g. as with endpoint corrected methods like Gregory quadrature [21]). Generally, we will not know the location of the discontinuities when applying these loop integral approximations in a symplectic diagnostic tool.

To decide which approximation scheme to use, one requires a priori knowledge of the regularity of the loop parameterization. A heuristic for selecting the appropriate loop integral approximation is as follows: for loops with Sobolev regularity $H^r(\mathbb{R}^{2d})$, where $r < 1$, one should use the finite-difference approximation, while, for $r \geq 1$, the pseudospectral approach converges faster.

Remark 4. *These results establish sufficient criteria for convergence. If the regularity of a given loop has been ascertained and an appropriate resolution has been used, then it is safe to conclude that the integral approximation may be trusted. However, because there may be uncertainty about the regularity of the loop data, and approximations to low-regularity loop integrals may converge slowly, it is frequently helpful to perform a parameter sweep to verify convergence.*

2.5 Approximating the loop integral as a function of time

In order to compute the approximate loop integral for multiple temporal snapshots of a simulation, it is necessary to consider how the regularity of an initially smooth loop in phase space deteriorates as the system evolves.

For a general autonomous ODE, $\dot{x} = F(x)$, over a compact n -dimensional manifold without boundary, M , with solution map $\Phi_t : M \rightarrow M$, if $F \in H^r(M)$, then one may show that $\Phi_t \in H^r(M)$ as a function of space [17]. (Here Φ_t denotes the true solution, not an approximation by some integration scheme.) Hence, given a Hamiltonian $\mathcal{H} \in H^r(\mathbb{T})$ for $r > 1$ and an initially smooth (e.g. C^∞) curve, γ , the curve evolves to a $H^{r-1}(\mathbb{T})$ curve, $\Phi_t^{\mathcal{H}} \circ \gamma$. In such a case, the approximate loop integral is guaranteed to converge when applied to successive snapshots of the solution. The least regular Hamiltonians considered in this work have piecewise linear potentials. Compactly supported piecewise linear functions on \mathbb{R} can be shown to be in $H^{3/2-\epsilon}(\mathbb{R}) \forall \epsilon > 0$, see appendix C. Hence, the least regular examples considered in this work admit convergent loop integral approximations if we use the finite difference approximation in these cases, but not if we approximate them using the pseudospectral approach.

For sufficiently regular Hamiltonians, convergence of the pseudospectral approximation is rapid enough that the loop integral can be approximated with relatively small ensembles parameterizing the loop. This is crucial since the approximation can be quite costly for high-dimensional systems: N_s independent simulations must be run to compute the loop integral. This is somewhat mitigated by the fact that these simulations can be done in parallel. Moreover, as we shall see subsequently, an effective way to monitor symplecticity conservation is to check the error incurred in the loop integral over a single time-step—likewise mitigating the cost.

As a final note, a distinction must be made between the exact flow map Φ_t and its approximation via a symplectic integrator. As we will see in section 4.2, certain low-regularity systems with symplectic continuous flow maps yield non-symplectic approximate flow maps when integrated with standard symplectic integrators like Strang splitting. The conservation or non-conservation of the loop integral over successive time-steps is entirely determined by the time-advance map used to generate the data at successive snapshots in time.

Remark 5. *The regularity of the Hamiltonian generating the flow determines the regularity of the loop which in turn determines the convergence rate of the loop integral approximations. Some delicacy is required, however, as the discrete-time flow obtained from a time-stepping method may not have the same spatial regularity as the continuous-time flow.*

Remark 6. *It is worth briefly highlighting how the approximate loop integral differs from energy as a computable figure of merit. To compute the approximate loop integral for a temporal simulation of a Hamiltonian system, N_s different simulations with initial data parameterizing the loop must be performed. This is in contrast with energy, which may be computed for a single trajectory. This is because symplecticity is a property associated with the geometry of phase-space and can only be measured with an ensemble of trajectories.*

3 A computable diagnostic for symplecticity

This section introduces the core contribution of this paper: a numerical diagnostic to monitor the conservation of symplecticity. Although applicable to any time-stepping method for Hamiltonian systems, the diagnostic is formulated as a tool for particle-in-cell methods. As such, special attention is given to difficulties arising when applying the tool to high-dimensional, low-regularity systems.

3.1 A diagnostic for symplecticity

Suppose that we evolve a phase-space loop in time, keeping track only of a finite number of sub-samples determined by the initial parameterization of the loop:

$$\{(\mathbf{q}_{k+1}(t), \mathbf{p}_{k+1}(t))\}_{k=0}^{N_s-1} \quad \text{such that} \quad (\mathbf{q}_{k+1}(0), \mathbf{p}_{k+1}(0)) = \gamma(k\Delta s), \quad (20)$$

for $k \in \{0, 1, 2, \dots, N_s - 1\}$, where $\Delta s = 1/N_s$. We may approximate the loop integral in time simply by applying one of the loop integral approximations from section 2.3 to the time-dependent loop. In the case of the pseudospectral approximation, we have

$$\mathcal{I}_N(t) = \mathbf{p}(t) : (\mathbb{D}\mathbf{q}(t))\Delta s = \sum_{i=1}^d \sum_{j,k=1}^{N_s} \mathbf{p}_{ki}(t) \mathbb{D}_{kj} \mathbf{q}_{ji}(t) \Delta s. \quad (21)$$

In the case of the finite difference approximation, we have

$$\mathcal{I}_N(t) = \sum_{i=1}^d \sum_{k \in K_i(L_q, L_p)} \mathbf{p}_{ik}(t) (\mathbf{q}_{i,k+1}(t) - \mathbf{q}_{ik}(t)). \quad (22)$$

While $\mathcal{I}(t) = \int \mathbf{p} \cdot d\mathbf{q}$ is conserved exactly by the flow, $\mathcal{I}_N(t)$ is conserved up to discretization error. The figure of merit considered in this work is the relative error incurred by the loop integral over a single time-step:

$$\mathcal{E}(h, N_s) = \left| \frac{\mathcal{I}_N(h) - \mathcal{I}_N(0)}{\mathcal{I}_N(0)} \right|. \quad (23)$$

For a Hamiltonian system with $2d$ degrees of freedom, if the time advance map is symplectic, then, for the pseudospectral approximation, we find that $\mathcal{E}(h, N_s) = O(dN_s^{-(2r-1)})$ uniformly in h , where r denotes the Sobolev regularity of the Hamiltonian function $\mathcal{H} \in H^r$, and for the finite difference approximation $\mathcal{E}(h, N_s) = O(dN_s^{-1})$. Hence, assuming the loop is adequately resolved, this figure of merit is a proxy for symplecticity conservation.

The diagnostic tool is defined as a parameter sweep in time-step size in which $\mathcal{E}(h, N_s)$ is computed for each value of h . To be specific:

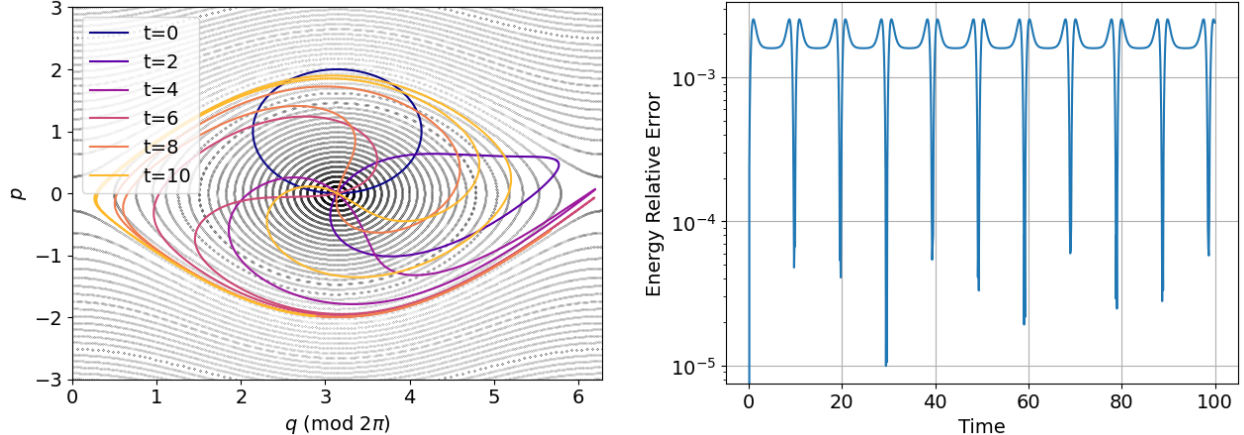
- To achieve R digits of accuracy, initialize a smooth loop in phase-space with
 - at least $N_s = O((d \times 10^R)^{1/(2r-1)})$ equispaced points for the pseudospectral approximation if the integrand is H^r with $r > 1/2$,
 - or with at least $N_s = O(d \times 10^R)$ equispaced points for the finite difference approximation if the integrand has low regularity.
- Compute $\mathcal{E}(h, N_s)$ for a range of time-steps $h = 2^{-m}$ for $m \in \{1, 2, \dots, M\}$.
- Plot the error versus time-step trend in log-log space.

A symplectic method should achieve R digits of accuracy regardless of time-step size, while a non-symplectic method will recover the convergence trend of the time-stepping method (with some caveats discussed below). Deviation from this expected behavior signals either that the integral was not properly resolved, in which case one should refine and try again, or that the method is not conserving the loop integrals—a signal that the method is not symplectic. Note that some experimentation may be needed to determine a suitable number of points since other factors (e.g. the local Lyapunov exponent of the flow) can limit convergence in addition to regularity.

It is possible that the integrator incurs errors in the loop integral diagnostic smaller than the number of digits a given simulation is capable of resolving. Integrators which conserve symplecticity up to $O(h^k)$, for some $k > 0$ are more challenging to distinguish from true symplectic integrators. Further, in low-regularity cases, an unreasonable number of points may be required to resolve the approximate loop integral to machine precision. In such cases, it is still possible to convincingly distinguish discretization errors from symplecticity errors by additionally running a convergence sweep in the parameter N_s with an extremely coarse time-step, e.g. $h = O(1)$. A true symplectic method exactly conserves the exact loop integral regardless of time-step size. The primary issue in these corner cases is distinguishing approximation error of the loop integral from errors in symplecticity conservation, and the large time-step amplifies potential errors in symplecticity preservation. If the expected error trend continues to the maximum resolution tested, either the method is symplectic, or the error in symplecticity is too small to be registered by the test. However, if the trend plateaus at a finite value above machine precision, then one has a source of error above and beyond discretization error, i.e. an error in symplecticity conservation for the time integration scheme itself.

3.2 Illustrative example: the shearing of phase-space loops

It is illustrative to look at the nonlinear pendulum, i.e. $\mathcal{H}(q, p) = p^2/2 + \sin(q)$. This system is especially nice since its Hamiltonian is C^∞ and the system is low dimensional. Therefore, this example serves to illustrate the difficulties the loop integral approximation can encounter in even the tamest systems. Because the flow is smooth, we use the pseudospectral method to approximate the loop integral. See Figure 1a for a visualization of the evolution of an initial loop under the time-advance map and 1b for the near conservation of energy by Strang splitting for a particular trajectory. See Figure 2 for the relative error in the approximate loop integral as a function of time



(a) Visualization of the deformation of an initially smooth loop by the nonlinear pendulum. (b) Energy conservation for trajectory starting at $(q_0, p_0) = (1, 0)$.

Figure 1: Visualization of the behavior of the nonlinear pendulum.

for two different initial loops. These figures demonstrate the severe shearing of the initial loop over time. Moreover, the number of points needed to resolve the approximate loop integral for a long simulation varies greatly depending on the location of the loop. However, in both case considered in Figure 2, if the loop is well-resolved initially, it remains well-resolved for at least a few time-steps before the shearing of phase-space causes issues. The behavior seen in this example is quite generic and motivates our definition of the diagnostic tool as a calculation over a single time-step. Of course, there may be utility in considering errors in the loop integral over longer simulations, but such considerations are outside the scope of this work.

3.3 Conservative, nearly-symplectic systems

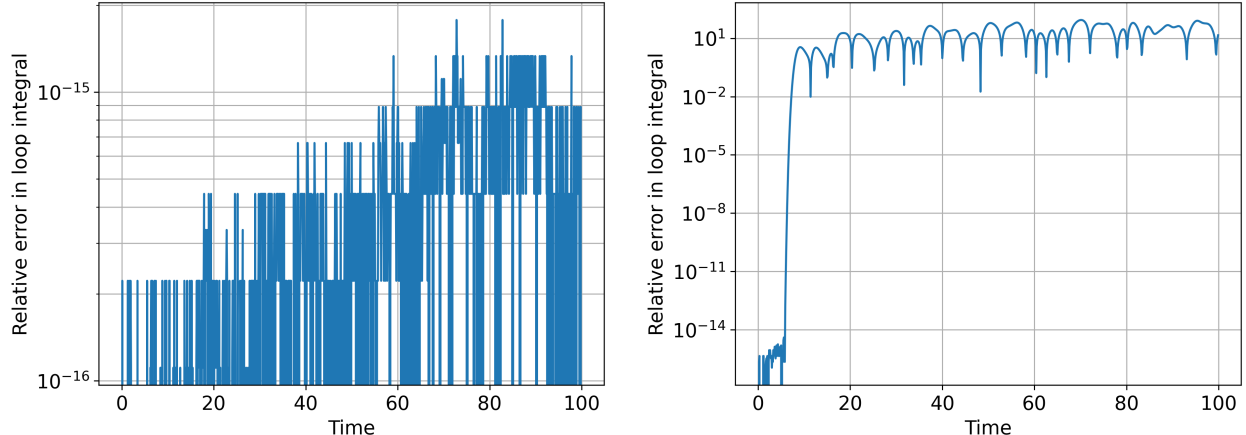
As mentioned previously, nearly-symplectic systems are particularly difficult to distinguish from symplectic systems using the numerical diagnostic. As such, it is worth highlighting a particularly well-known case of near-symplecticity to alert the reader that extra care may be needed when studying such time-steppers. A family of non-symplectic time-stepping methods known as conjugate symplectic methods nearly conserve the Poincaré integral invariants over long simulations [37]. If Φ_h^{CS} is the flow of the conjugate symplectic method, there exists a symplectic map, Φ_h^S , and a near-identity formal diffeomorphism, χ_h , such that

$$\Phi_h^{CS} = \chi_h^{-1} \circ \Phi_h^S \circ \chi_h. \quad (24)$$

By near-identity, we mean that $\chi_h(\mathbf{z}) = \mathbf{z} + O(h^p)$ for some $p \geq 1$. Such methods can be shown to possess long-time near-symplecticity:

$$|(D_{\mathbf{z}}\Phi_h^{CS})^T J_c D_{\mathbf{z}}\Phi_h^{CS} - J_c| = O(h^p). \quad (25)$$

An example of a conjugate symplectic method is the leapfrog method (which staggers position and momentum updates in time): this method differs from Strang splitting (or Störmer-Verlet) by a half-timestep. Certain energy-conserving methods, including the popular averaged vector field discrete gradient method [48], have been shown to possess a slightly weakened form of conjugate symplecticity [26]. This work compares only Strang splitting (an explicit symplectic method) and



(a) Approximate loop integral as a function of time. (b) Approximate loop integral as a function of time. Initial loop of radius 1 centered at $(q_0, p_0) = (\pi, 1/2)$. Initial loop of radius 1 centered at $(q_0, p_0) = (0, 0)$.

Figure 2: Comparison of approximate loop integral conservation by the nonlinear pendulum for two different initial loops.

second-order explicit Runge-Kutta (RK2) as a baseline for comparison. Conjugate symplectic and energy conserving methods are outside the scope of this work. However, the performance of the diagnostic on these systems is of substantial interest and worth pursuing in a future work.

4 On the symplecticity of low regularity Hamiltonian systems

We now consider the symplecticity of flow maps of low regularity Hamiltonian systems and the symplecticity of their discrete-time approximation. We find that Hamiltonian systems with discontinuous vector fields, even when their continuous-time flow is symplectic, yield discrete-time flow maps which are generally not symplectic when approximated using Hamiltonian splitting methods. This is notable, because Hamiltonian systems with piecewise linear potentials, commonly found in PIC methods, fall into this category. In particular, the classic and ubiquitous *cloud-in-cell* scheme uses linear shape functions [4, 30, 55]. Many structure-preserving particle-in-cell methods, while designed to be compatible with shape-functions of general polynomial degree, do not explicitly disallow the use of linear shape functions [38, 22, 23, 6, 42]. Finally, it is not just piecewise linear interpolation which is a problem: any interpolation scheme which does not yield a globally C^1 interpolant, e.g. PIC methods with field discretizations based on C^0 finite elements [3, 22, 23, 20] or Lagrange interpolation [35], will suffer from the same issues described in this section. The following discussion demonstrates the pathological behavior of such systems in a simple model problem.

4.1 Interpretation of flow maps for low-regularity Hamiltonian systems

Given a Hamiltonian system with

$$\mathcal{H}(q, p) = \frac{1}{2}p^2 + V(q), \quad (26)$$

where $V(q)$ is only piecewise smooth, the associated Hamiltonian vector field has jump discontinuities. Consequently, the classical existence and uniqueness theory for ODEs does not apply, and one

must adopt a notion of weak solution. We interpret the flow as the limit of a sequence of smooth Hamiltonian systems

$$\mathcal{H}_\epsilon(q, p) = \frac{1}{2}|p|^2 + V_\epsilon(q), \quad (27)$$

where $V_\epsilon \in C^\infty(\mathbb{R}^d)$ and $V_\epsilon \rightarrow V$ uniformly away from the jump set (e.g., $V_\epsilon = V * \eta_\epsilon$ with a standard mollifier η_ϵ). In this sense, the mollified flows Φ_ϵ^t converge to a limiting flow Φ^t that is defined for almost every initial condition and preserves the measure-theoretic properties of the phase space. This construction aligns with the notion of regular Lagrangian flow [1], which rigorously defines solution maps for ODEs generated by vector fields of bounded variation.

To our knowledge, the conservation of the Poincaré integral invariant in the regular Lagrangian flow framework has not been studied in the literature. Intuitively, preservation of the Poincaré integral invariant is tied to the preservation of phase space loop topology. The continuous-time flow of a piecewise smooth Hamiltonian system preserves the topology of loops, provided the initial loop excludes points that approach the jump set tangentially (where the Hamiltonian vector field is discontinuous). In many practical cases, this set of problematic initial conditions has zero Lebesgue measure. For example, if V is piecewise smooth with jump sets that are C^1 hypersurfaces, then tangential approaches to the jump set are exceptional: they occur only if the gradient of the potential is locally parallel to the normal of the hypersurface. Hence, we expect that the Poincaré integral invariant may be conserved for a large class of low-regularity Hamiltonian systems interpreted in the sense of a regular Lagrangian flow, even though a full rigorous proof is not yet available.

4.2 Hamiltonian splitting flow maps for piecewise linear potentials

Consider the canonical Hamiltonian system generated by the Hamiltonian $\mathcal{H}(q, p) = p^2/2 + |q|$:

$$\begin{aligned} \dot{q} &= p, \\ \dot{p} &= -\text{sign}(q). \end{aligned} \quad (28)$$

The system is formally equivalent to the model of a particle falling in a uniform gravitational potential which experiences a perfect elastic collision with the boundary $q = 0$, and parabolic trajectories for $q > 0$. Such a system is known as a hybrid system [16] (so named because it possesses qualities of both continuous and discrete dynamical systems), and its flow may be shown to preserve the symplectic form. For this system, if we consider trajectories which remain within a compact subset of \mathbb{R}^2 (e.g. trajectories near the origin), we may cut off the potential in a smooth manner without affecting the dynamics. Thus, the Hamiltonian is $H^{3/2-\epsilon}(\mathbb{R}^2)$, $\forall \epsilon > 0$. Hence, the finite difference loop integral approximation would converge for this system, but not the pseudospectral approximation. In what follows, we show that even the exact loop integrals fail to be conserved over a single time-step by Hamiltonian splitting time-advance maps.

Given a general Hamiltonian system with $\mathcal{H}(q, p) = K(p) + V(q)$, the most basic Hamiltonian splitting method, the Lie-Trotter method, is obtained from the partial flow maps,

$$\Phi_h^K(q, p) = (q + h\nabla K(p), p), \quad \text{and} \quad \Phi_h^V(q, p) = (q, p - h\nabla V(q)), \quad (29)$$

which are obtained by exactly integrating the Hamiltonian system while alternately setting the kinetic or potential energy to zero over a single time-step, h . The two $O(h)$ Lie-Trotter update maps are defined to be

$$\Phi_h^q(q, p) = \Phi_h^V \circ \Phi_h^K(q, p), \quad \text{or} \quad \Phi_h^p(q, p) = \Phi_h^K \circ \Phi_h^V(q, p), \quad (30)$$

where Φ_h^q might be called the *position-first update*, and Φ_h^p the *momentum-first update*. When applied to Hamiltonian systems with sufficient regularity, these Lie-Trotter update rules are symplectic maps, and higher-order splitting methods, such as Strang-splitting, may be obtained as compositions of basic steps of this form [27].

Suppose that one wishes to integrate the original absolute value potential system using Hamiltonian splitting. The partial flow-maps are given by

$$\Phi_h^K(q, p) = (q + hp, p), \quad \text{and} \quad \Phi_h^V(q, p) = (q, p - h \operatorname{sign}(q)). \quad (31)$$

We now examine whether the Lie-Trotter flow maps Φ_h^q and Φ_h^p are symplectic when applied to this particular system. Evidently, the flow maps are discontinuous along the line $q = 0$, so the formula $D_z \Phi_h^T J_c D_z \Phi_h = J_c$ may only be verified, and indeed holds, away from $q = 0$. We can, however, check what happens to conservation of loop integrals when this discontinuity is encountered.

Define the phase-space loop $\gamma : \mathbb{R} \bmod 2\pi \rightarrow \mathbb{R}^2 : \theta \mapsto (\sin(\theta), \cos(\theta))$. Note that

$$\int_{\gamma} p \mathrm{d}q = \int_0^{2\pi} \cos^2(\theta) \mathrm{d}\theta = \pi. \quad (32)$$

Composing this loop with the update maps, one finds

$$\Phi_h^q \circ \gamma(\theta) = (\sin(\theta) + h \cos(\theta), \cos(\theta) - h \operatorname{sign}(\sin(\theta) + h \cos(\theta))), \quad (33)$$

and

$$\Phi_h^p \circ \gamma(\theta) = (\sin(\theta) + h(\cos(\theta) - h \operatorname{sign}(\sin(\theta))), \cos(\theta) - h \operatorname{sign}(\sin(\theta))). \quad (34)$$

The curve $\Phi_h^q \circ \gamma(\theta)$ has discontinuities where $\sin(\theta) + h \cos(\theta) = 0$, i.e. at

$$\tan(\theta) = -\frac{1}{h} \implies \theta \in \{\pi - \arctan(1/h), 2\pi - \arctan(1/h)\}. \quad (35)$$

The curve $\Phi_h^p \circ \gamma(\theta)$ has discontinuities $\theta \in \{0, \pi, 2\pi\}$. We compute integrals over these deformed loops by only integrating over the continuous sub-intervals of each curve. Doing so, one finds that

$$I_1(h) = \int_{\Phi_h^q \circ \gamma} p \mathrm{d}q = \pi - \frac{4h(1 - h^2)}{\sqrt{1 + h^2}}, \quad \text{and} \quad I_2(h) = \int_{\Phi_h^p \circ \gamma} p \mathrm{d}q = \pi + 4h^2. \quad (36)$$

As $h \rightarrow 0$, one recovers the expected value of π . However, for any finite time-step, one incurs an $O(h^2)$ error in the loop integral value. Similarly, if one defines the Strang splitting updates to be:

$$\Phi_h^{q,S} = \Phi_{h/2}^K \circ \Phi_h^V \circ \Phi_{h/2}^K, \quad \text{and} \quad \Phi_h^{p,S} = \Phi_{h/2}^V \circ \Phi_h^K \circ \Phi_{h/2}^V, \quad (37)$$

then it may be shown that

$$\int_{\Phi_h^{q,S} \circ \gamma} p \mathrm{d}q = \pi + \frac{4h^2}{\sqrt{h^2 + 4}}, \quad \text{and} \quad \int_{\Phi_h^{p,S} \circ \gamma} p \mathrm{d}q = \pi - h^3 + 2h^2. \quad (38)$$

The flow maps obtained from higher order splitting methods are likewise expected to fail to conserve the loop integral.

As previously mentioned, we can show that the continuous-time flow conserves symplecticity. For the Hamiltonian $\mathcal{H}(q, p) = \frac{1}{2}p^2 + |q|$, the Hamiltonian vector field is smooth except on a measure-zero set ($q = 0$). On any smooth portion of the flow, the standard Hamiltonian theory guarantees local conservation of the symplectic form. Moreover, the level sets of \mathcal{H} are continuous

curves in phase space (parabolas glued at $q = 0$), and the flow is continuous in time. Therefore, a topological loop advected by the flow remains a continuous curve, provided we exclude from the initial conditions the exceptional set for which the flow is undefined (i.e., $(q, p) = (0, 0)$). Since the flow preserves the local symplectic form and advects the loop continuously, Stokes' theorem implies that the loop integral is invariant under the flow. The key distinction between the continuous-time flow and the discrete flows obtained from Hamiltonian splitting in this example is that the continuous-time flow map enjoys spatial continuity while the discrete flow maps do not.

This simple example illustrates a problem which is generically present in symplectic PIC with piecewise linear interpolation and Strang-splitting time-stepping. Indeed, one can manufacture a case in which a given particle effectively experiences this potential, see appendix E. Because the approximate time-advance map implied by Hamiltonian splitting yields a discontinuous map in phase-space, crossings of cell-boundaries cause topological loops to break, leading to a loss of conservation of the Poincaré integral invariant. It is worth emphasizing that we expect the continuous-time flow of the piecewise linear PIC system to be symplectic, as with this simple example. However, the discontinuous character of the discrete-time flow maps obtained from Hamiltonian splitting methods for these systems results in the breaking of topological loops. In general, one should not expect PIC methods with piecewise linear interpolation and explicit, Hamiltonian-splitting time-advance maps to preserve symplecticity. Higher-order interpolation is needed.

Remark 7. *We saw in this example that spatial continuity of the flow map is essential to ensure the conservation of the Poincaré loop integral invariant in low regularity flows. It is reasonable to ask why we take such pains to design a loop integral approximation which is convergent for discontinuous loops. The reason is the non-equivalence of the spatial regularity of the exact and approximate flow maps, as seen in this example: while the continuous-time flow may preserve loop continuity, a discrete or approximate flow can still fail to do so. Having a convergent symplectic diagnostic is therefore important to detect conservation reliably, even when it is not obvious whether a given time-stepping scheme preserves the spatial continuity of the underlying continuous flow.*

More specifically, pseudospectral approximations of the loop integral fail to converge for loops with minimal regularity $q, p \in H^{1/2+\epsilon}$ (for small $\epsilon > 0$), which is just enough regularity to guarantee continuity. In contrast, a finite-difference loop integral approximation remains applicable and convergent even when the loop data is discontinuous. This allows us to distinguish between cases where the flow truly preserves the loop integral and cases where a numerical approximation fails due to insufficient spatial regularity.

4.3 Example: an interpolated nonlinear pendulum

This example considers a coarse-grained version of a potential which interpolates its values on a uniform grid with spacing, Δq . The polynomial basis used to approximate the potential are B-splines. This basis is used because it ensures differentiability up to the polynomial degree used: a degree- p B-spline is C^{p-1} . This allows us to directly test the behavior of the loop integral diagnostic when applied to Hamiltonian systems of specified regularity. The piecewise character of potentials also mimics those encountered in particle-in-cell methods which will be considered subsequently.

Let $q_i = i\Delta q, \forall i \in \mathbb{Z}$. In one spatial dimension, the constant and linear B-spline basis functions may be written as follows:

$$B_i^0(q) = \begin{cases} 1, & q \in [q_i, q_{i+1}] \\ 0, & \text{else,} \end{cases} \quad \text{and} \quad B_i^1(q) = \begin{cases} \frac{\Delta q - |q - q_{i+1}|}{\Delta q}, & q \in [q_i, q_{i+2}] \\ 0, & \text{else,} \end{cases} \quad (39)$$

The higher-order B-splines are obtained via convolutions of the lower-order B-splines:

$$B_i^\alpha(q) = \underbrace{(B_i^0 * B_i^0 * \cdots * B_i^0)}_{\alpha+1 \text{ times}}(q) = B_i^0 * B_i^{\alpha-1}(q). \quad (40)$$

Notice, this increases the width of the degree- α basis function to encompass $\alpha + 1$ cells. The Hamiltonian with an interpolated potential is written as

$$\mathcal{H}(q, p) = \frac{p^2}{2} + V_{\Delta q}^\alpha(q), \quad (41)$$

where

$$V_{\Delta q}^\alpha(q) = \sum_{j=i-\alpha+1}^{i+1} V_j B_j^\alpha(q) \quad \text{for } q \in [q_i, q_{i+1}], \quad (42)$$

where the coefficients V_i are selected so that $V_{\Delta q}^\alpha(q_i) = V(q_i)$.

In this example, we use $V(q) = \sin(q) + \cos^2(2q + 1)$, and $\Delta q = 2\pi/25 \approx 0.25$. The large grid spacing helps to ensure that issues with symplecticity preservation due to low regularity, if they are present, are sufficiently exaggerated so as to readily appear in the numerical results. The symplecticity of the algorithm does not depend on the magnitude of Δq , so this choice does not influence the the conclusions drawn from the numerical tests. Tests are performed using $\alpha = 1, 2, 3$, and for the original, non-interpolated potential. The loop is initialized as a circle of radius 1 centered at $(q_0, p_0) = (\pi, 0)$. The cases with $\alpha = 2, 3$, and the original, non-interpolated potential enjoy high enough regularity that the pseudospectral loop integral approximation converges. The case $\alpha = 1$ uses the finite difference loop integral approximation.

See Figure 3 for the relative error in the symplectic diagnostic over a single time-step as a function of N_s , the number of points resolving the loop, using a fixed time-step size of $\Delta t = 0.1$. This parameter sweep serves to verify that the loop integral approximations are converging with the expected rate. Indeed, the convergence rates roughly correspond with the order of polynomial interpolation for the Strang splitting integrator. In all cases, RK2 achieves an $O(10^{-3})$ error. In the test where $\alpha = 1$, both Strang-splitting and RK2 saturate about 10^{-3} . Strang splitting is not expected to be symplectic in the case $\alpha = 1$ due to the low regularity of the Hamiltonian, so this result is expected.

See Figure 4 for the relative error in the loop integral over a single time-step as a function of time-step size, Δt , with $N_s = 2^{16}$ points approximating the loop in the cases $\alpha = 3$ and the non-interpolated case, and $N_s = 2^{20}$ points in the cases $\alpha = 1, 2$. In these tests which use the pseudospectral loop integral approximation, this is more than enough resolution to eliminate discretization error: indeed, in the case $\alpha = 3$, the approximation should get 14 decimal places of accuracy with about $N_s = (10^{14})^{1/4} \approx 3162$ points. For $\alpha = 2$, we use $2^{20} = 1,048,576$ which guarantees about 13 decimal places of accuracy. The finite difference approximation in the case $\alpha = 1$ cannot be expected to converge to machine precision. Even with $2^{20} = 1,048,576$ points, only 6 digits of accuracy are expected. This is sufficient to see that the performance of Strang-splitting and RK2 is largely indistinguishable. For the finite difference loop integral approximation, the parameters detecting jumps are set to $L_q = L_p = 10$, because large discontinuities are not expected. One can see that, in each case, the error incurred in the loop integral by RK2 follows a convergence trend as the time-step is refined, whereas Strang splitting in the non-interpolated and $\alpha = 2, 3$ test cases robustly conserve the diagnostic for all time-step sizes. Interestingly, in all cases except $\alpha = 1$, the convergence trend in Δt for the error incurred by RK2 appears to have a slope of Δt^4 , rather than the expected slope of Δt^2 . The sweep in Δt in the piecewise linear case indicates a

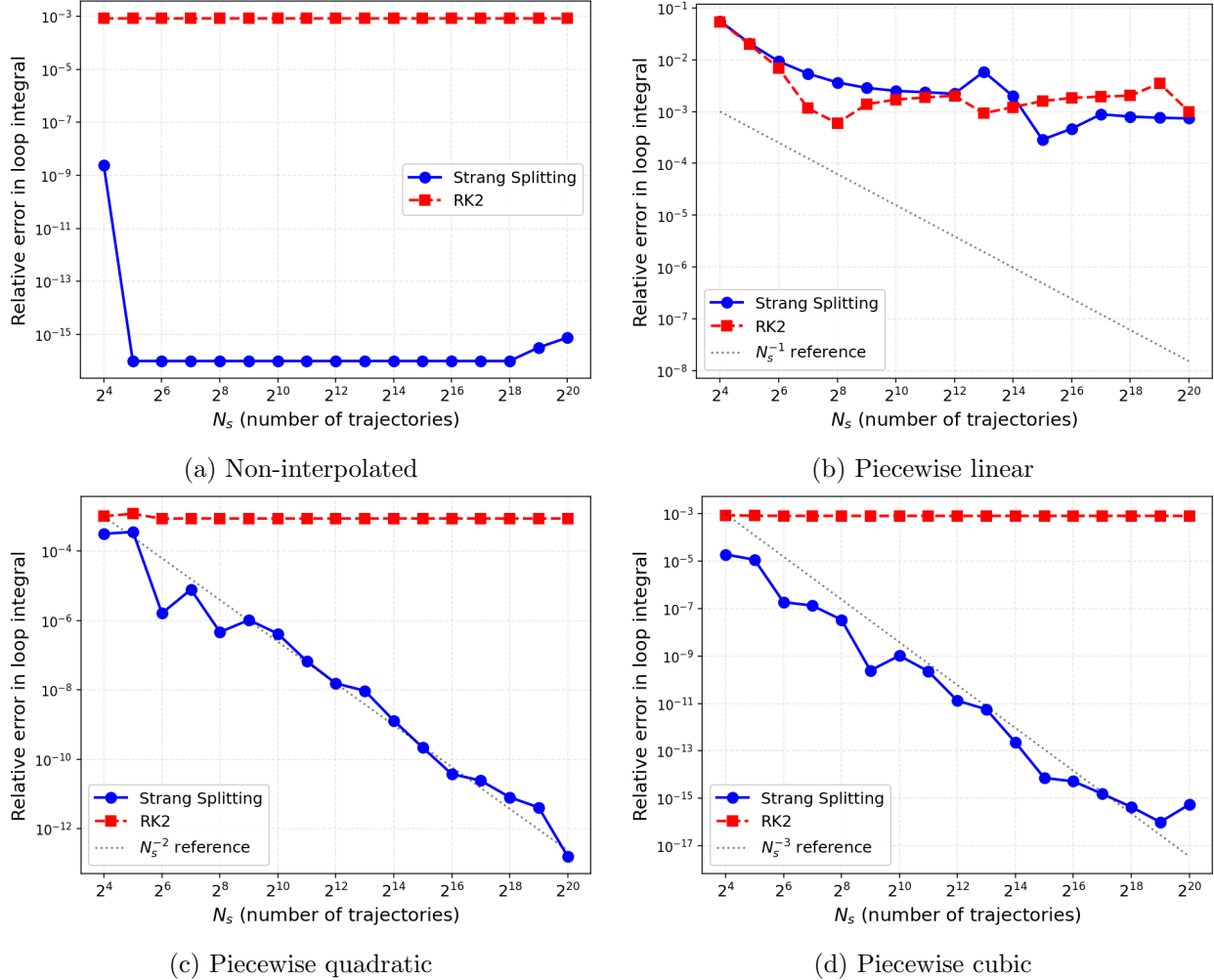


Figure 3: Interpolated potential conservation results. Sweep in the number of points approximating the loop. The approximation of the diagnostic for the linear case saturates at an error of about 10^{-6} , indicating a failure to converge the symplectic diagnostic.

failure to conserve symplecticity: Strang splitting and RK2 perform comparably in conservation of the loop integral. Note that we only trust the results in this test for time-step sizes coarse enough that discretization error is smaller than the error in symplecticity: i.e. for Δt greater than about 2^{-6} . The tests $\alpha = 2, 3$ and the non-interpolated case all indicate symplecticity conservation. Note, the case $\alpha = 2$ is only accurate to about 13 decimal places due to discretization error.

4.4 Example: a nonlinear pendulum array

We next consider how the diagnostic performs when applied to a high dimensional system with a real analytic Hamiltonian. Consider a row of N equispaced nonlinear pendula, each coupled to its neighbors by linear Hookean springs. The position coordinates $\{q_i\}_{i=1}^N$ are the positions of the particles relative to their resting position. The evolution equations are then given by

$$\ddot{q}_i = \alpha_i \sin(q_i) + k_i(q_{i-1} - q_i - \Delta q_{i-1}) + k_{i+1}(q_{i+1} - q_i + \Delta q_i), \quad i = 1, \dots, N, \quad (43)$$

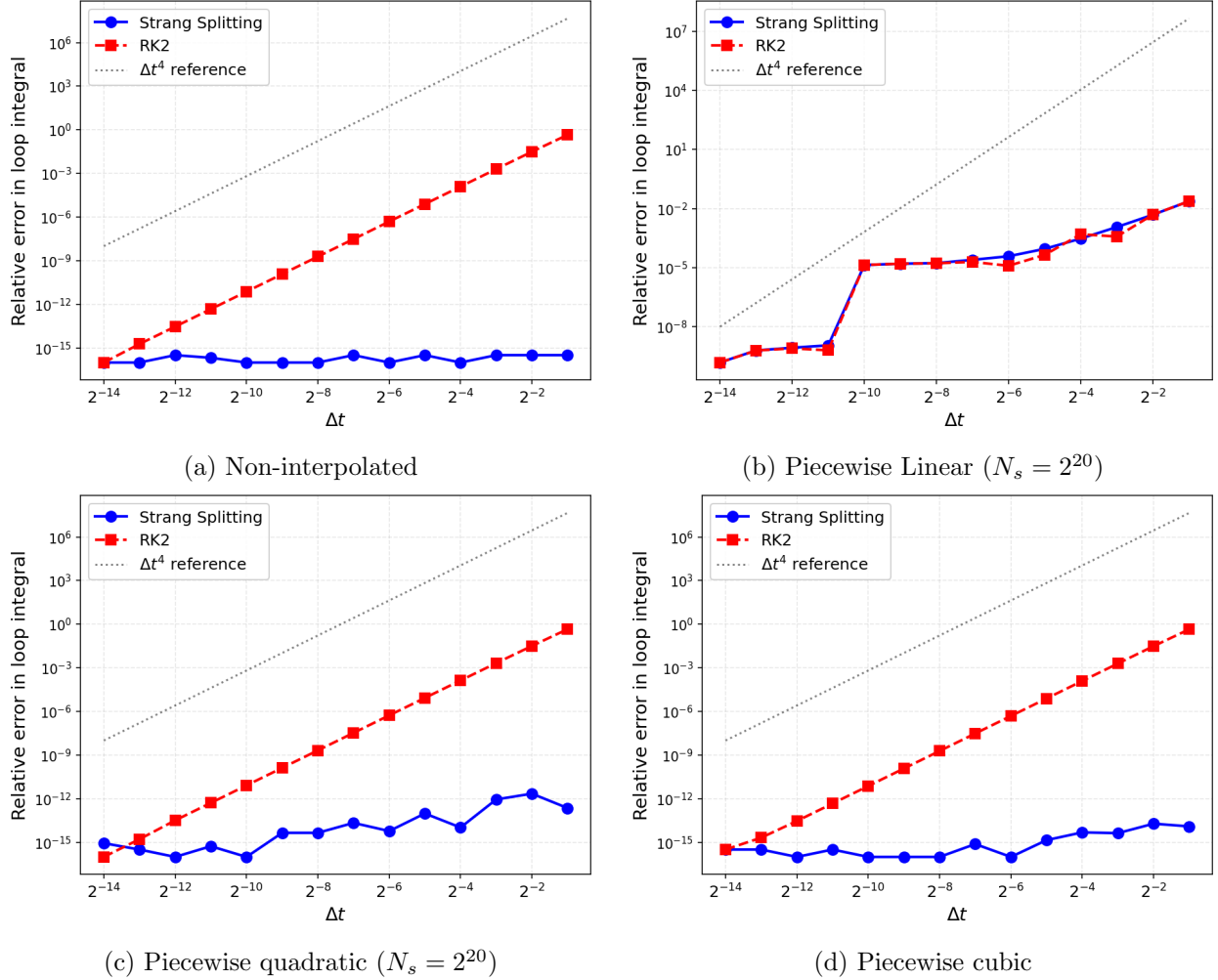


Figure 4: Interpolated potential conservation results. Sweep in the time-step size.

where α_i is the spring constant for the i^{th} pendulum, k_i is the spring constant for the spring connecting the $(i-1)^{th}$ and i^{th} pendulums, and Δq_i is the difference between the rest positions of pendulum i and $i+1$. For simplicity, we assume that $\alpha_i = \alpha > 0$, $k_i = k > 0$, and $\Delta q_i = \Delta q \forall i$. Further, we let the first and last springs couple with each other so that $q_{N+1} = x_1$ and $x_0 = x_N$: i.e., the array is arranged in a ring. Hence, the evolution equations become

$$\ddot{q}_i = \alpha \sin(q_i) + k(q_{i+1} - 2q_i + q_{i-1}), \quad i = 1, \dots, N. \quad (44)$$

This evolution equation comes from the Lagrangian

$$L(q_i, \dot{q}_i) = \sum_{i=1}^N \left(\frac{1}{2} \dot{q}_i^2 - \alpha \cos(q_i) + \frac{1}{2} k q_i (-q_{i+1} + 2q_i - q_{i-1}) \right). \quad (45)$$

The Lagrangian may be written in vector notation as follows:

$$L(\mathbf{q}, \dot{\mathbf{q}}) = \frac{1}{2} \dot{\mathbf{q}}^T \dot{\mathbf{q}} - \alpha \mathbb{1}^T \cos(\mathbf{q}) - \frac{1}{2} k \mathbf{q}^T \mathbb{L} \mathbf{q}, \quad (46)$$

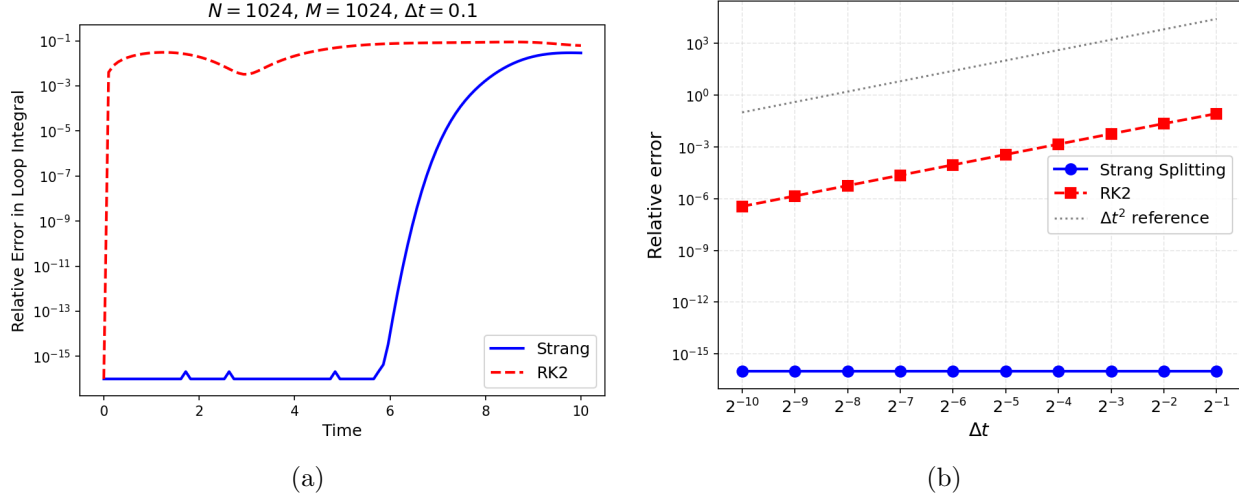


Figure 5: Results for nonlinear pendulum array test.

where $\mathbb{1} = (1, 1, \dots, 1)$, and \mathbb{L} is the circulant matrix with stencil $(-1, 2, -1)$. Alternatively, this may be modeled as a canonical Hamiltonian system with Hamiltonian:

$$\mathcal{H}(\mathbf{q}, \mathbf{p}) = \frac{1}{2} \mathbf{p}^T \mathbf{p} + \alpha \mathbb{1}^T \cos(\mathbf{q}) + \frac{1}{2} k \mathbf{q}^T \mathbb{L} \mathbf{q}, \quad (47)$$

which yields the evolution equations

$$\dot{\mathbf{p}} = \alpha \sin(\mathbf{q}) - k \mathbb{L} \mathbf{q}, \quad \dot{\mathbf{q}} = \mathbf{p}. \quad (48)$$

This system may be thought of as a finite difference approximation of the one-dimensional Sine-Gordon equation if we let $k = \Delta q^{-2}$. In the tests considered here, $\alpha = k = 1$, and the initial conditions are generated as uniform random numbers in the interval $[0, 1]$. The loop for computing the diagnostic is generated by periodically perturbing these random initial conditions along a circle of radius 1. As the Hamiltonian is C^∞ , the pseudospectral loop integral approximation is applicable, and converges rapidly. See Figure 5a for the relative error in the loop integral as a function of time. See Figure 5b for the relative error in the symplectic diagnostic over a single time-step as a function time-step, Δt , using $N = 4096$ pendulums and $N_s = 4096$ points in the loop integral. The diagnostic is well-resolved across the parameter sweep with a modest number of points resolving the loop (relative to system size) due to the analyticity of the Hamiltonian.

4.5 Discussion

The tests in this section confirm that it is regularity of the Hamiltonian, and not dimensionality, which limits the applicability of the loop integral diagnostic. The loop integral diagnostic is easy to resolve to machine precision with a modest number of sample points if the Hamiltonian is smooth, and, conversely, a large number of points are needed in cases of low regularity. The flow maps arising from Hamiltonian splitting methods applied to piecewise linear Hamiltonians fail to conserve the loop integral diagnostic, indicating that these flow maps are not symplectic.

These observations lead to the conclusion that Hamiltonian splitting methods should not be used to temporally integrate Hamiltonian systems with piecewise linear interpolated fields, these, respectively, being staple temporal [38, 29] and spatial [4, 30, 55] approximation methods in PIC. Note that structure-preserving PIC methods are generally not limited to linear shape functions,

and indeed frequently use high-order shape functions in their practical numerical tests. However, they do offer the option of using linear shape functions as a viable choice in the algorithm. That the use of linear shape functions leads to a violation of symplecticity preservation appears to be absent in the structure-preserving PIC literature. Perhaps more importantly, it further follows that PIC methods which use higher-order interpolation which nonetheless does not yield a globally C^1 interpolant, such as standard C^0 finite element PIC methods [3, 22, 23, 20] or methods based on Lagrange interpolation/histopolation [35], will likewise suffer from this issue. Regarding symplecticity preservation, structure-preserving PIC methods based higher order B-spline [38, 7] or Fourier interpolation [19, 7, 52, 44] are highly favorable since these yield a globally high-order interpolant.

The Section 5 will further explore these claims by applying the diagnostic to a structure-preserving particle-in-cell method.

5 Symplectic electrostatic particle-in-cell methods

The use of the symplectic diagnostic to study the preservation of symplecticity in electrostatic particle-in-cell (PIC) methods presents two difficulties. First, these systems are high-dimensional and expensive to simulate. Therefore, it is desirable to use as few trajectories to approximate the loop integral as possible. Second, the regularity of the Hamiltonian in a symplectic PIC method is limited by the degree of polynomial interpolation used when depositing charge to the grid. This forces one to use more points to approximate the loop integral.

The system of interest in this section is the Vlasov-Poisson system (with physical constants set to unity):

$$\partial_t f + \mathbf{v} \cdot \nabla_{\mathbf{x}} f - \nabla \phi \cdot \nabla_{\mathbf{v}} f = 0, \quad -\Delta \phi = \rho_0 - \int f d\mathbf{v}, \quad (49)$$

where ρ_0 is a neutralizing background charge density. This system is Hamiltonian [40, 43] with Poisson bracket

$$\{F, G\} = \int f \left[\frac{\delta F}{\delta f}, \frac{\delta G}{\delta f} \right] d\mathbf{x} d\mathbf{v}, \quad [f, g] = \nabla_{\mathbf{x}} f \cdot \nabla_{\mathbf{v}} g - \nabla_{\mathbf{x}} g \cdot \nabla_{\mathbf{v}} f, \quad (50)$$

and Hamiltonian

$$\mathcal{H}[f] = \int \left(\int \frac{1}{2} |\mathbf{v}|^2 f(\mathbf{x}, \mathbf{v}) d\mathbf{v} + \rho(\mathbf{x}) \phi(\mathbf{x}) \right) d\mathbf{x}, \quad \text{where} \quad -\Delta \phi = \rho_0 - \int f d\mathbf{v}. \quad (51)$$

We consider only periodic boundary conditions in space.

5.1 Symplectic PIC methods

Many structure-preserving PIC methods have been derived based on the Hamiltonian or variational structure of the Vlasov equation [53, 47, 38, 45, 56, 19, 29, 7, 22, 23, 46, 35, 51, 54, 47, 34, 33, 6, 42]. Following the general approach described in these prior works, one may obtain an electrostatic PIC method for the Vlasov-Poisson system written as a nearly-canonical Hamiltonian system which captures many salient features common to these structure-preserving PIC methods. The Hamiltonian is given by

$$\mathcal{H}(\mathbf{x}_1, \mathbf{v}_1, \dots, \mathbf{x}_N, \mathbf{v}_N) = \frac{1}{2} \left(\sum_{a=1}^{N_p} w_a |\mathbf{v}_a|^2 + \boldsymbol{\rho}^T \mathbb{L}^{-1} \boldsymbol{\rho} \right), \quad \text{where} \quad \rho_i = \rho_0 - \sum_a w_a B_i^p(\mathbf{x}_a), \quad (52)$$

for some piecewise interpolating polynomial basis $\{B_i^p\}$ with \mathbb{L} being the discrete Laplacian matrix associated with the basis, and where $(\mathbf{x}_a, \mathbf{v}_a) \in \mathbb{R}^{2d}$ are the position and velocity of the a^{th} particle and w_a is its weight. The Poisson bracket is given by

$$\{F, G\} = \sum_{a=1}^{N_p} \frac{1}{w_p} \left(\frac{\partial F}{\partial \mathbf{x}_a} \cdot \frac{\partial G}{\partial \mathbf{v}_a} - \frac{\partial G}{\partial \mathbf{x}_a} \cdot \frac{\partial F}{\partial \mathbf{v}_a} \right). \quad (53)$$

Only the constant scaling factor in the bracket prevents this system from being canonical. The evolution equations are given by

$$\begin{aligned} \mathbf{x}_a &= \{\mathbf{x}_a, \mathcal{H}\} = \mathbf{v}_a \\ \mathbf{v}_a &= \{\mathbf{v}_a, \mathcal{H}\} = \mathbf{E}_h(\mathbf{x}_a) = -\nabla \phi_h(\mathbf{x}_a), \end{aligned} \quad (54)$$

where

$$(\mathbb{L}\Phi)_i = \rho_0 - \sum_a w_a B_i^p(\mathbf{x}_a) \quad \text{and} \quad \phi_h(\mathbf{x}) = \sum_i \phi_i B_i^p(\mathbf{x}). \quad (55)$$

The discrete Laplacian matrix is computed as the finite element stiffness matrix associated with the basis: $\mathbb{L}_{ij} = (\nabla B_i^p, \nabla B_j^p)_{L^2}$. We interpolate with p^{th} order B-splines over a uniform grid, hence the notation for the basis functions. In one spatial dimension, the domain is $\Omega = [0, L]$, and with N grid-points, the grid-spacing is $\Delta x = L/N$. The B-spline basis functions are constructed as described in Equations (39) and (40). A basis in higher dimensions may be obtained as a tensor product of the one-dimensional basis.

As in the rest of this paper, we temporally integrate using Strang splitting:

$$\begin{aligned} \mathbf{x}_a^{n+1/2} &= \mathbf{x}_a^n + \frac{\Delta t}{2} \mathbf{v}_a^n, \\ \mathbf{v}_a^{n+1} &= \mathbf{v}_a^n - \Delta t \nabla \phi_h(\mathbf{x}_a^{n+1/2}), \\ \mathbf{x}_a^{n+1} &= \mathbf{x}_a^{n+1/2} + \frac{\Delta t}{2} \mathbf{v}_a^{n+1}. \end{aligned} \quad (56)$$

By doing the velocity update second, only a single field solve is needed per time-step. As in the rest of the paper, for comparison, we consider the non-symplectic second-order explicit Runge-Kutta (RK2) method. This section considers only the 1D1V PIC method for simplicity since the behavior of the diagnostic may be readily seen in this simplified setting.

5.2 Applying the symplectic diagnostic to PIC

The Landau damping and two-stream instability test cases are used as initial conditions for the simulations. For Landau damping, the initial positions are sampled from the distribution:

$$f_x(x) \propto 1 + A \cos(2\pi kx/L), \quad (57)$$

where $A \in (0, 1)$, and $k \in \{1, 2, \dots\}$. The initial velocities are sampled from a normal distribution:

$$f_v(v) \propto \exp\left(-\frac{v^2}{v_{th}^2}\right). \quad (58)$$

For the two-stream instability, the initial conditions are $x_a \sim U([0, L])$, a uniform distribution on $[0, L]$, and v_a are sampled with the density:

$$f_v(v) \propto \exp\left(-\frac{(v - v_b)^2}{v_{th}^2}\right) + \exp\left(-\frac{(v + v_b)^2}{v_{th}^2}\right) \quad (59)$$

where v_b is the velocity of the counter-propagating beams, and v_{th} is the width of the beams (the thermal speed). We seed the instability by periodically perturbing each particle velocity:

$$\tilde{v}_a = (1 + A \sin(2\pi x_a/L))v_a. \quad (60)$$

For our tests, we consider a domain of length $L = 50$, $v_{th} = 1$, $v_{nb} = 3$, $A = 0.5$, and $k = 1$. The particle weights are made to be uniform such that the charge density is unity.

Let N_s be the number of samples to resolve the loop, and let N_p be the number of particles in each simulation. For $p = 1$, linear interpolation, we must use the finite difference loop integral approximation, while for $p = 2, 3$, we use the pseudospectral loop integral approximation. To allow for possibly large gradients in the loop, we set $L_q = L_p = 1000$ in the finite difference loop integral approximation (and hence only converge for $N_s > 1000$). See figure 6 for the convergence of the single-step loop integral error as a function of N_s with fixed $\Delta t = 0.1$ and $N_p = 128$. For $p = 1$, we do not observe the convergence trend, because $L_q = L_p = 1000$, and the quadrature error has already saturated for $N_s > 1000$. For $p = 2$, we observe a convergence rate trend of N_s^{-2} . For $p = 3$, we observe a convergence rate trend of N_s^{-3} , which is slightly lower than what theory would predict if the Hamiltonian indeed has spatial regularity of $H^{3+1/2-\epsilon}$.

These results inform the parameters to use for the Δt sweep. We expect an error of about $O(N_p/N_s)$ in the case $p = 1$. If we use $N_p = 2$ and $N_s = 2^{15}$, we can expect about five decimal places of accuracy. In the case $p = 2$, we can expect nine digits of accuracy with $N_p = 2$ and $N_s = 2^{15}$. In the case $p = 3$, we can expect fourteen digits of accuracy with $N_p = 2$ and $N_s = 2^{15}$. Such small number of particles (while entirely inappropriate in a PIC simulation) is beneficial in testing symplecticity. The conservation/non-conservation of symplecticity does not depend on the physical realism of the simulation.

See Figure 7 for the relative error in the symplectic diagnostic over a single time-step as a function of Δt selecting N_s and N_p as described as above. Due to a lack of spatial continuity, the approximate flow map from the piecewise linear, $p = 1$, PIC method fails to be symplectic, and no discernible difference in loop integral conservation can be found between Strang-splitting and RK2. In the piecewise quadratic and cubic test cases, we expect about 9 and 14 digits of accuracy, respectively. This is roughly observed in the numerical results. Strang-splitting in both tests enjoy loop integral conservation within about two or three orders magnitude of machine precision, and only modest reduction in error as the timestep is refined. This is in contrast with RK2, which clearly follows a convergence trend as the time-step decreases. This, combined with the results reported in Figure 6 strongly support the conclusion that these algorithms are symplectic, as expected.

See Figure 8 for a visualization of the relative error in the energy as a function of time. In all cases, energy is conserved well on average despite the linear case failing to conserve the loop integral diagnostic.

5.3 The effects of smoothing in PIC methods

A common feature of PIC methods is smoothing via some kind of filtering operation [4, 30, 14]. These filters are introduced to reduce noise in the simulation by smoothing out the charge distribution prior to solving Poisson's equation. Binary filtering takes local averages in a moving window. Such filtering may be incorporated into the Hamiltonian structure as follows: given the circulant binary filtering matrix

$$\mathbb{B}_{ij} = \begin{cases} 1/2, & i = j \\ 1/4, & |i - j| = 1 \\ 0, & \text{else,} \end{cases} \quad (61)$$

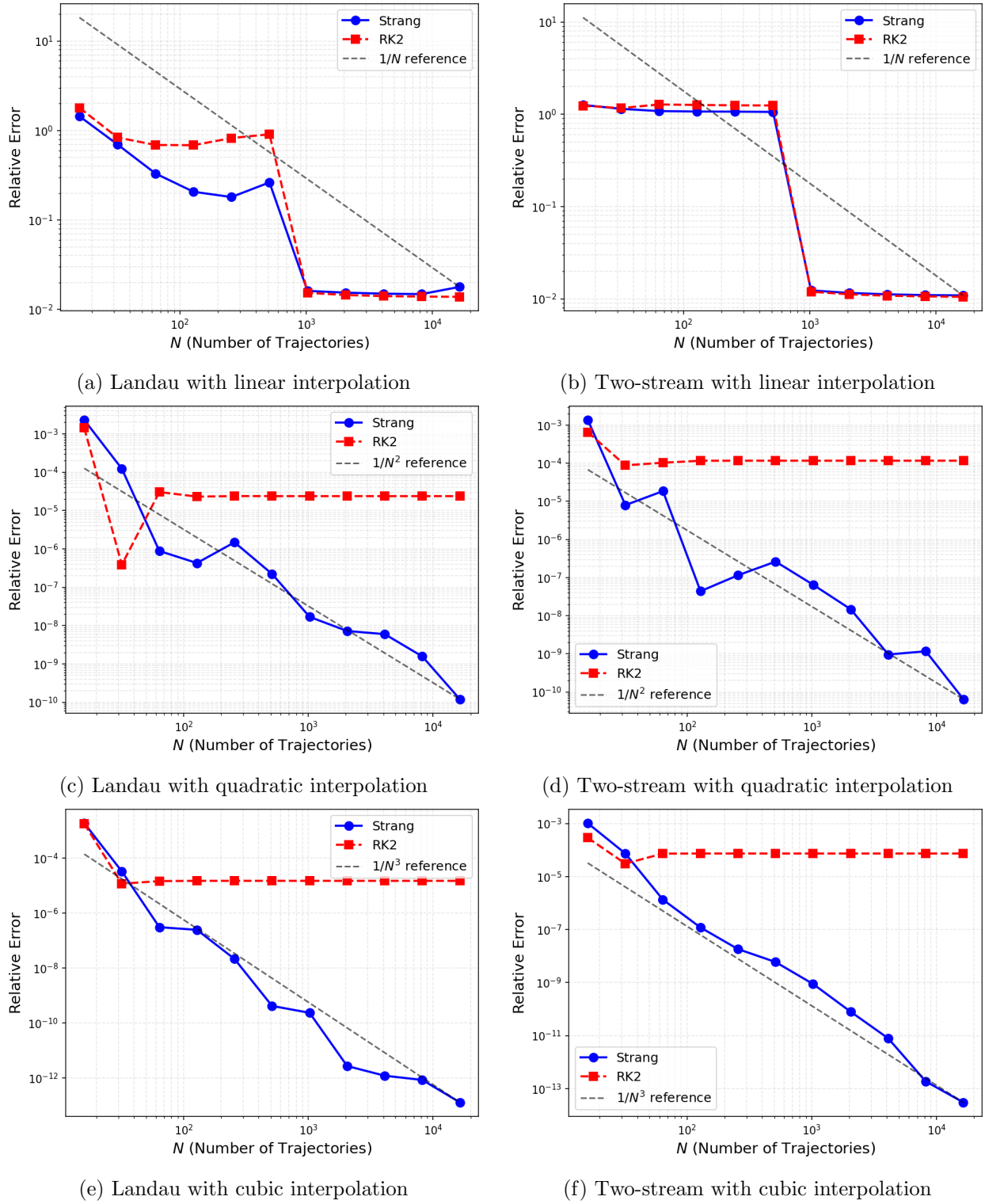
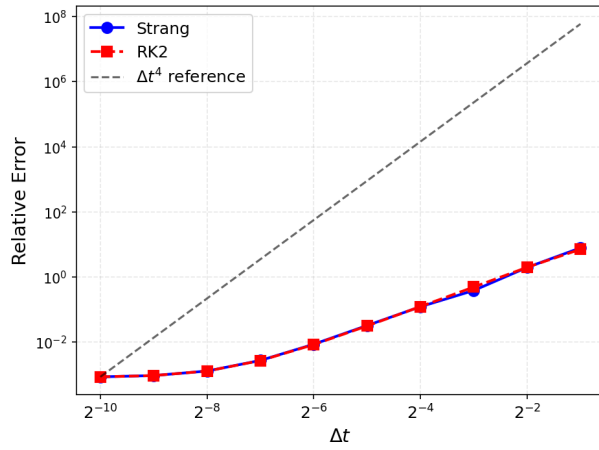
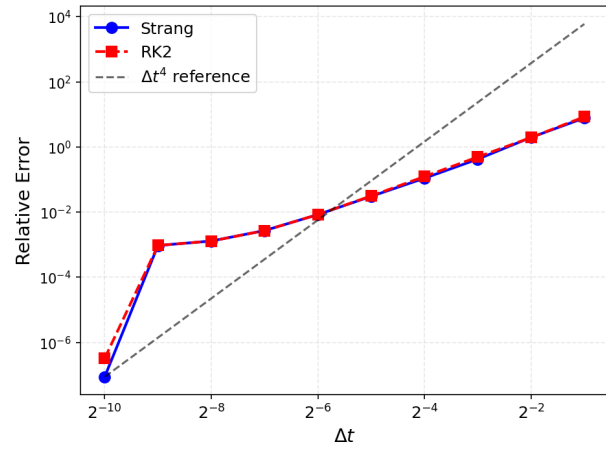


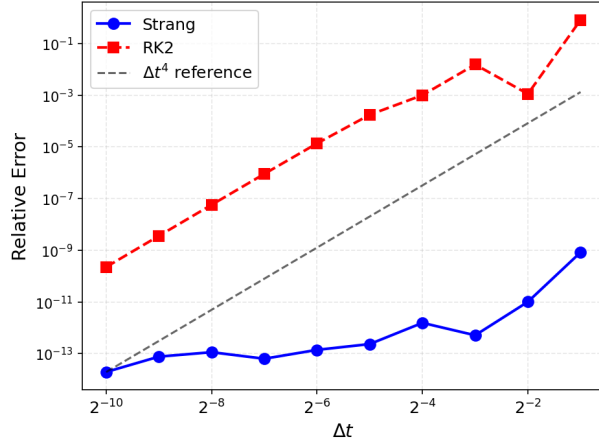
Figure 6: Convergence trends as a function of N_s with $\Delta t = 0.1$, and $N_p = 128$.



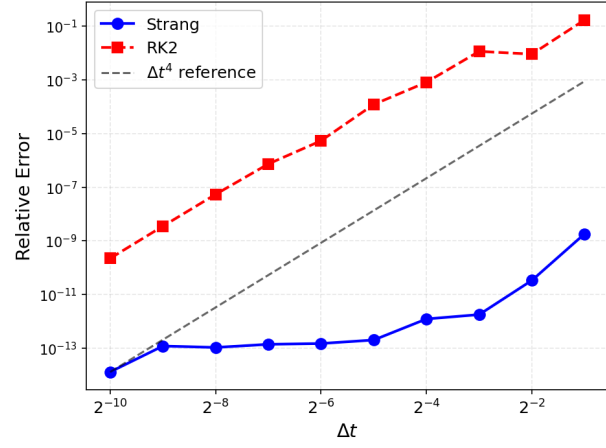
(a) Landau with linear interpolation



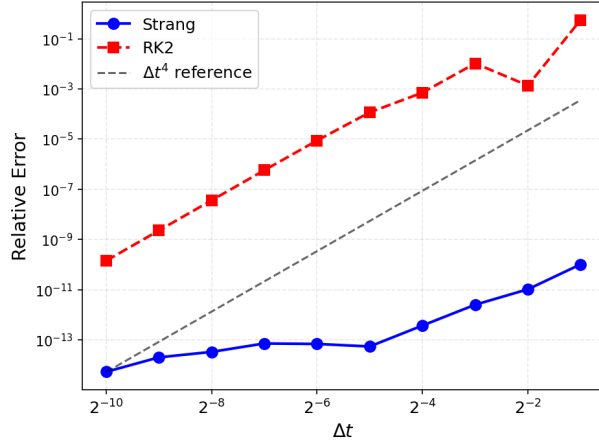
(b) Two-stream with linear interpolation



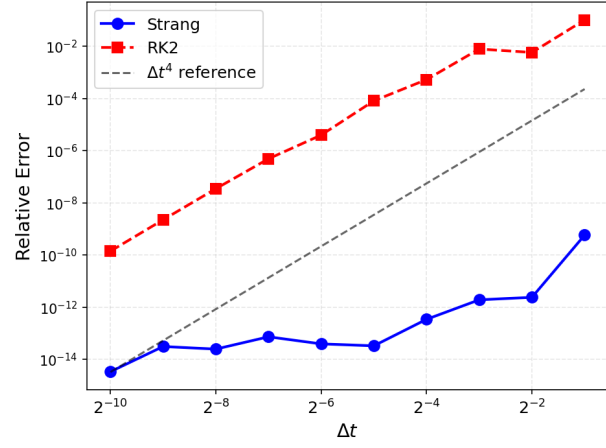
(c) Landau with quadratic interpolation



(d) Two-stream with quadratic interpolation



(e) Landau with cubic interpolation



(f) Two-stream with cubic interpolation

Figure 7: Convergence trends of single-step loop integral errors as a function of Δt . These tests used 128 grid points on a domain of length $L = 50$, with $N_p = 2$ particles, and $N_s = 32,768$ points to resolve the loop integrals.

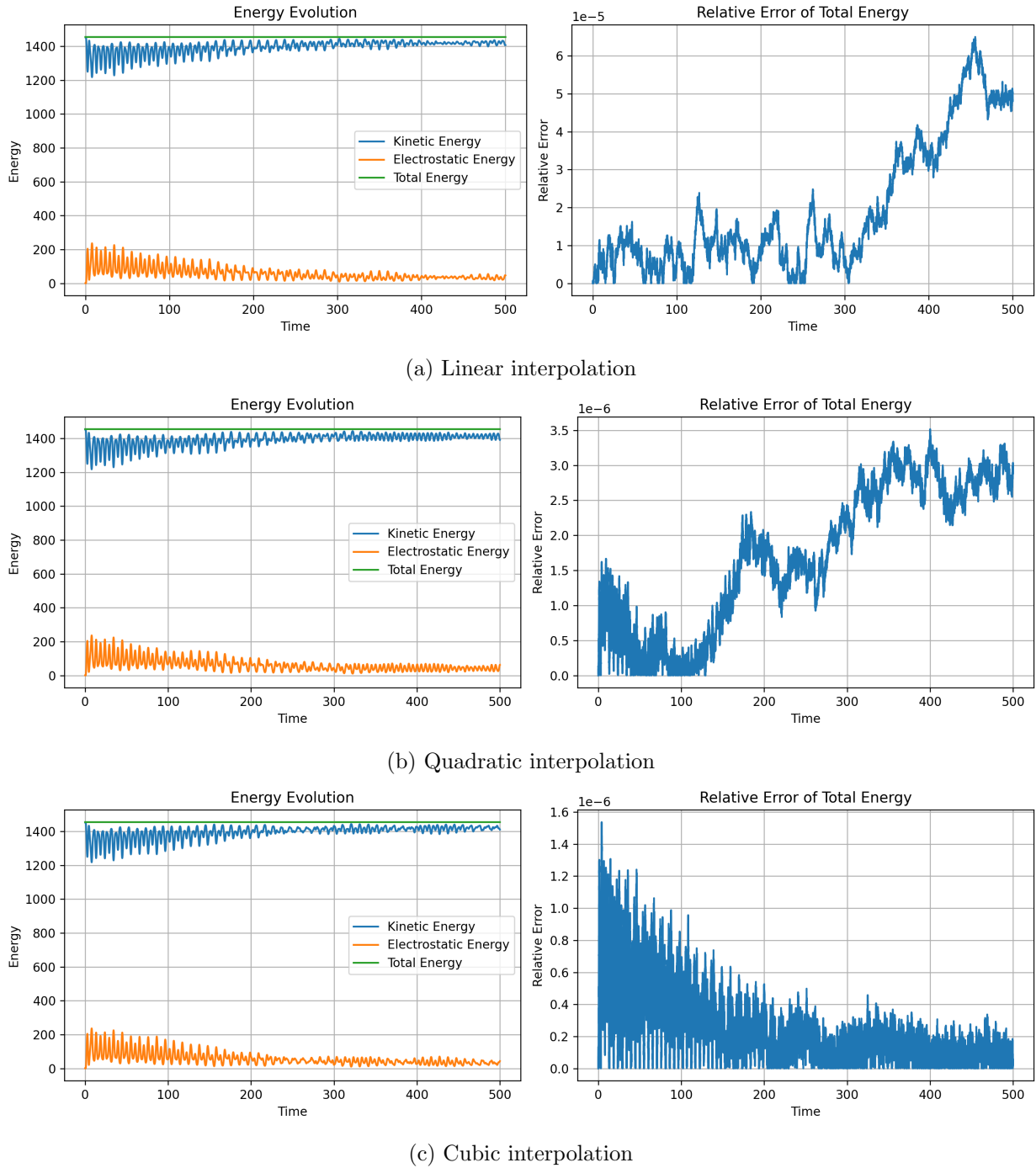


Figure 8: Energy conservation results for two-stream instability PIC simulations. These used $N_x = 200$ grid points, domain length $L = 50$, time-step $\Delta t = 0.01$, and $N_p = 10,000$ particles.

the Hamiltonian is modified as follows:

$$\mathcal{H}(\mathbf{x}_1, \mathbf{v}_1, \dots, \mathbf{x}_N, \mathbf{v}_N) = \frac{1}{2} \left(\sum_{a=1}^{N_p} w_a |\mathbf{v}_a|^2 + \boldsymbol{\rho}^T \mathbb{L}^{-1} \mathbb{B}^s \boldsymbol{\rho} \right), \quad \text{where } \rho_i = \rho_0 - \sum_a w_a B_i^p(\mathbf{x}_a), \quad (62)$$

where

$$\mathbb{B}^s = \underbrace{\mathbb{B} \mathbb{B} \dots \mathbb{B}}_{s \text{ times}}. \quad (63)$$

Hence, the filter is simply a post-processing step when depositing charge to the grid, applied prior to computing the electrostatic potential. With periodic boundary conditions and a uniform grid, both \mathbb{B}^s and \mathbb{L}^{-1} are circulant matrices. Hence, the two matrices commute. This is because circulant matrices generically commute with each other [31], indeed they are diagonalized by the discrete Fourier transform matrix. Therefore, although the notation does not make the fact explicit, the potential energy is still a symmetric positive semi-definite quadratic form in $\boldsymbol{\rho}$. This filtering operation does not fundamentally alter the continuity of the Hamiltonian since the potential is still just a p^{th} -degree B-spline. However, smoothing should decrease the size of the discontinuities in the p^{th} derivative as it effectively widens the interpolation stencil.

Conjunctly increasing s and N so that their ratio remain in a fixed relationship effectively approximates smoothing by a Gaussian kernel. In Fourier space, the filter is given by:

$$\widehat{\mathbb{B}}(k) = \frac{1}{2} + \frac{1}{2} \cos(k\Delta x) \implies (\widehat{\mathbb{B}}(k))^s = \left(\frac{1}{2} + \frac{1}{2} \cos(k\Delta x) \right)^s. \quad (64)$$

For $k\Delta x \ll 1$, that is for the low wave-numbers, we obtain:

$$(\widehat{\mathbb{B}}(k))^s \approx \left(1 - \frac{1}{4}(k\Delta x)^2 \right)^s. \quad (65)$$

For large s , using the limit $(1 - x/s)^s \approx e^{-x}$, this expression approaches:

$$\widehat{\mathbb{B}}_\infty(k) = \exp \left(- \left(\frac{k}{2\sigma} \right)^2 \right), \quad \text{where } \sigma = \sqrt{s}\Delta x. \quad (66)$$

Transforming back to physical space, the filter remains Gaussian. Hence, even though smoothing does not eliminate the problem of limited regularity from low order polynomial interpolation in PIC, one might reasonably hope that sufficiently aggressive smoothing effectively mitigates the problem in an asymptotic sense. The following tests examine this supposition.

See figure 9 for the relative error in the symplectic diagnostic over a single time-step as a function of Δt for $s = 0, 2$, and 4 applications of filtering for the linear and quadratic interpolation cases. The cubic interpolation test case is omitted since the results are entirely analogous to the quadratic case. We find that filtering reduces errors in the loop integral diagnostic slightly in the quadratic case, but has almost no effect in the linear case. Filtering most likely achieves two things: it modifies the convergence trend in N_s allowing the loop integral approximation to converge to its true value more quickly, and also slightly reduces the magnitude of the error in the loop integral diagnostic incurred over a single time-step. The convergence rate of the approximation of the loop integral improves if the data is more regular (e.g. if the loop data has a smaller Lipschitz constant). However, filtering does not change the differentiability of the function, and therefore has limited impact as far as symplecticity conservation is concerned.

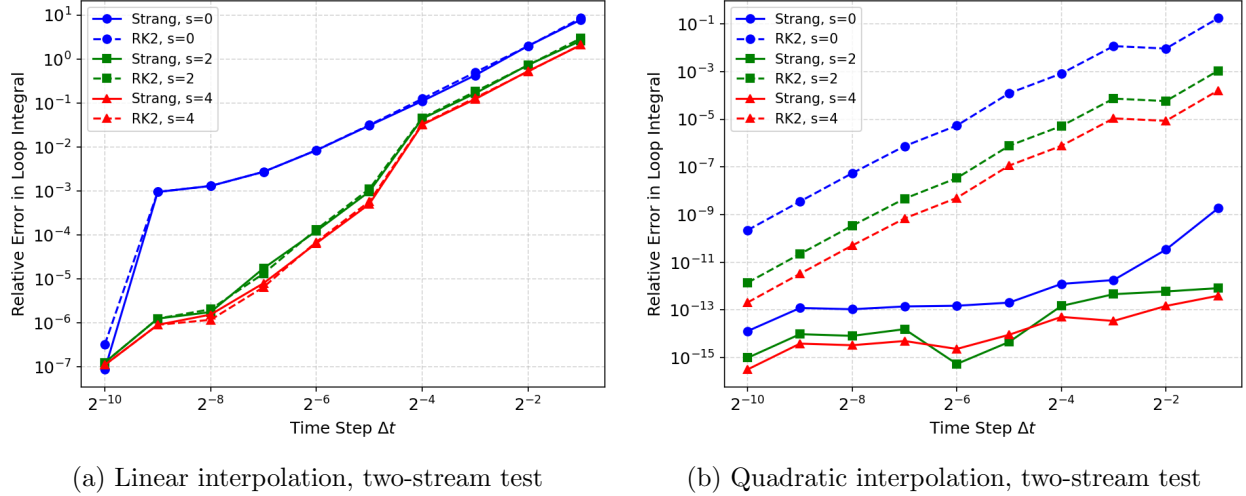


Figure 9: Convergence trends of single-step loop integral errors as a function of Δt with binary filtering. These tests used 128 grid points on a domain of length $L = 50$, $\Delta t = 0.1$, with $N_p = 2$ particles, and $N_s = 32,768$ points to resolve the loop integrals.

6 Conclusion

This paper proposes a diagnostic tool for symplectic integration, with a particular emphasis on its use with symplectic PIC methods. While a diagnostic of this kind previously appeared in [37], this work specifically considered how it works in relation with Hamiltonians of limited regularity and applied the diagnostic to study the symplecticity of structure-preserving particle-in-cell methods. The diagnostic converges spectrally, however, this convergence rate is limited by the regularity of the Hamiltonian vector field. Due to this limitation, the diagnostic is most useful when applied to Hamiltonian systems with a high degree of regularity, but may nonetheless be used for low regularity systems if a sufficiently high resolution is used.

The key finding of this work is that “symplectic” PIC methods which use piecewise linear interpolation do not, in fact, preserve symplecticity. Indeed, PIC methods which use explicit time-stepping and any interpolation which fails to be globally C^1 also fail to preserve symplecticity. This problem is not ameliorated by standard filtering techniques. Rather, to have a truly symplectic PIC method, one must ensure continuous differentiability of the Hamiltonian. In electrostatic PIC, this corresponds to requiring that the electrostatic potential be interpolated in a globally C^1 basis. One may reasonably expect a similar principle to apply for electromagnetic PIC methods with time-stepping based on Hamiltonian splitting [29, 38]. For the purposes of efficiently resolving the loop integral diagnostic, cubic or higher interpolation is preferable to quadratic interpolation, as the diagnostic converges with a smaller ensemble of simulations. Furthermore, while B-splines are conventional in PIC, and this work used B-splines, it is not unknown to use Lagrange or other forms of polynomial interpolation [35], especially in finite element PIC methods [3, 22, 23, 20]. One should be careful in such cases, as other forms of polynomial interpolation do not link interpolation degree with global regularity in such a direct manner as B-splines: e.g. degree- $(p + 1)$ Lagrange interpolation on a non-uniform grid does not automatically yield a C^p interpolant. The results herein show that continuous differentiability of the Hamiltonian is a necessary condition for the flow map to be symplectic when approximated with standard splitting methods. Therefore, true symplectic PIC methods require more than a compatible choice of basis functions for the fields and a symplectic time-stepper. Regularity of the basis across cell interfaces is also crucial.

This work exclusively considered explicit symplectic integration based on Strang splitting, as this form of time-stepping is conventional in many structure-preserving PIC algorithms. Implicit time-stepping methods are beyond the scope of this work, and may or may not admit symplectic algorithms with low-order spatial regularity. Such implicit symplectic integrators are a topic of particular interest for future work. The sensitivity of symplecticity preservation to solver tolerance is worth investigating. The conservation of the Poincaré integral invariant by conjugate symplectic methods is likewise of interest. Finally, the performance of the diagnostic in energy conserving PIC methods [14, 13, 12, 15, 11, 10, 49, 36, 32], which are a significant thrust in contemporary PIC literature, is of interest. The desire to distinguish symplectic and conservative, non-symplectic PIC methods was a core motivation for developing this diagnostic tool, and will be considered in subsequent work.

Acknowledgements

This material is based on work supported by the U.S. Department of Energy, Office of Science, Office of Advanced Scientific Computing Research, as a part of the Mathematical Multifaceted Integrated Capability Centers program, under Award Number DE-SC0023164. It was also supported by U.S. Department of Energy grant # DE-FG02-04ER54742. WB was supported by the Laboratory Directed Research and Development program of Los Alamos National Laboratory under project number 20251151PRD1. Los Alamos Laboratory Report LA-UR-25-31632.

Code Availability

The source code to reproduce all the results found in this paper is publicly available on GitHub at: https://github.com/wbarham/symplectic_diagnostic. This repository also serves as a template for using the diagnostic in other contexts.

References

- [1] L. Ambrosio. “Transport equation and Cauchy problem for BV vector fields.” In: *Inventiones mathematicae* 158.2 (2004).
- [2] J. Bernier, F. Casas, and N. Crouseilles. “Splitting methods for rotations: application to vlasov equations, to appear in SIAM J”. In: *Sci. Comp.*, hal-02178952 () .
- [3] M. T. Bettencourt et al. “EMPIRE-PIC: a performance portable unstructured particle-in-cell code”. In: *Communications in Computational Physics* 30.SAND-2021-2806J (2021).
- [4] C. K. Birdsall and A. B. Langdon. *Plasma physics via computer simulation*. CRC press, 2018.
- [5] J. P. Boyd. *Chebyshev and Fourier spectral methods*. Courier Corporation, 2001.
- [6] J. W. Burby. “Finite-dimensional collisionless kinetic theory”. In: *Physics of Plasmas* 24.3 (2017).
- [7] M. Campos Pinto, K. Kormann, and E. Sonnendrücker. “Variational framework for structure-preserving electromagnetic particle-in-cell methods”. In: *Journal of Scientific Computing* 91.2 (2022), p. 46.
- [8] F. Casas et al. “High-order Hamiltonian splitting for the Vlasov–Poisson equations”. In: *Numerische Mathematik* 135.3 (2017), pp. 769–801.

- [9] E. Celledoni et al. “Energy-preserving runge-kutta methods”. In: *ESAIM: Mathematical Modelling and Numerical Analysis* 43.4 (2009), pp. 645–649.
- [10] L. Chacón and G. Chen. “A curvilinear, fully implicit, conservative electromagnetic PIC algorithm in multiple dimensions”. In: *Journal of computational physics* 316 (2016), pp. 578–597.
- [11] L. Chacón, G. Chen, and D. C. Barnes. “A charge-and energy-conserving implicit, electrostatic particle-in-cell algorithm on mapped computational meshes”. In: *Journal of Computational Physics* 233 (2013), pp. 1–9.
- [12] G. Chen and L. Chacon. “A multi-dimensional, energy-and charge-conserving, nonlinearly implicit, electromagnetic Vlasov–Darwin particle-in-cell algorithm”. In: *Computer Physics Communications* 197 (2015), pp. 73–87.
- [13] G. Chen and L. Chacón. “An energy-and charge-conserving, nonlinearly implicit, electromagnetic 1D-3V Vlasov–Darwin particle-in-cell algorithm”. In: *Computer Physics Communications* 185.10 (2014), pp. 2391–2402.
- [14] G. Chen, L. Chacón, and D. C. Barnes. “An energy-and charge-conserving, implicit, electrostatic particle-in-cell algorithm”. In: *Journal of Computational Physics* 230.18 (2011), pp. 7018–7036.
- [15] G. Chen et al. “A semi-implicit, energy-and charge-conserving particle-in-cell algorithm for the relativistic Vlasov–Maxwell equations”. In: *Journal of Computational Physics* 407 (2020), p. 109228.
- [16] W. Clark and A. Bloch. “Invariant forms in hybrid and impact systems and a taming of Zeno”. In: *Archive for Rational Mechanics and Analysis* 247.2 (2023), p. 13.
- [17] D. G. Ebin and J. Marsden. “Groups of diffeomorphisms and the motion of an incompressible fluid”. In: *Annals of Mathematics* 92.1 (1970), pp. 102–163.
- [18] L. Evans and R. Gariepy. *Measure Theory and Fine Properties of Functions, Revised Edition*. Textbooks in Mathematics. CRC Press, 2015.
- [19] E. G. Evstafiev and B. A. Shadwick. “Variational formulation of particle algorithms for kinetic plasma simulations”. In: *Journal of Computational Physics* 245 (2013), pp. 376–398.
- [20] D. S. Finn et al. “A numerical study of landau damping with petsc-pic”. In: *Communications in Applied Mathematics and Computational Science* 18.1 (2023), pp. 135–152.
- [21] B. Fornberg and J. A. Reeger. “An improved Gregory-like method for 1-D quadrature”. In: *Numerische Mathematik* 141.1 (2019), pp. 1–19.
- [22] A. S. Glasser and H. Qin. “A gauge-compatible Hamiltonian splitting algorithm for particle-in-cell simulations using finite element exterior calculus”. In: *Journal of Plasma Physics* 88.2 (2022), p. 835880202.
- [23] A. S. Glasser and H. Qin. “Generalizing Yee’s method: Scalable geometric higher-order FEEC algorithms for Maxwell’s equations on an unstructured mesh”. In: *arXiv preprint arXiv:2301.01753* (2023).
- [24] O. Gonzalez. “Time integration and discrete Hamiltonian systems”. In: *Journal of Nonlinear Science* 6.5 (1996), pp. 449–467.
- [25] D. Gottlieb and S. A. Orszag. *Numerical analysis of spectral methods: theory and applications*. SIAM, 1977.

[26] E. Hairer. “Energy-Preserving Variant of Collocation Methods”. In: *JNAIAM* 5.1-2 (2010), pp. 73–84.

[27] E. Hairer, C. Lubich, and G. Wanner. *Geometric numerical integration*. Second. Vol. 31. Springer Series in Computational Mathematics. Structure-preserving algorithms for ordinary differential equations. Springer-Verlag, Berlin, 2006, pp. xviii+644.

[28] P. Hartman. *Ordinary differential equations*. SIAM, 2002.

[29] Y. He et al. “Hamiltonian time integrators for Vlasov–Maxwell equations”. In: *Physics of Plasmas* 22.12 (2015).

[30] R. W. Hockney and J. W. Eastwood. *Computer simulation using particles*. crc Press, 2021.

[31] R. A. Horn and C. R. Johnson. *Matrix analysis*. Cambridge university press, 2012.

[32] L. Ji et al. “An asymptotic-preserving and energy-conserving particle-in-cell method for Vlasov–Maxwell equations”. In: *Journal of Mathematical Physics* 64.6 (2023).

[33] X. Jianyuan and Q. Hong. “Explicit structure-preserving geometric particle-in-cell algorithm in curvilinear orthogonal coordinate systems and its applications to whole-device 6D kinetic simulations of tokamak physics”. In: *Plasma Science and Technology* 23.5 (2021), p. 055102.

[34] X. Jianyuan, Q. Hong, and L. Jian. “Structure-preserving geometric particle-in-cell methods for Vlasov–Maxwell systems”. In: *Plasma Science and Technology* 20.11 (2018), p. 110501.

[35] K. Kormann and E. Sonnendrücker. “A Dual Grid Geometric Electromagnetic Particle in Cell Method”. In: *SIAM Journal on Scientific Computing* 46.5 (2024), B621–B646.

[36] K. Kormann and E. Sonnendrücker. “Energy-conserving time propagation for a structure-preserving particle-in-cell Vlasov–Maxwell solver”. In: *Journal of Computational Physics* 425 (2021), p. 109890.

[37] M. Kraus. *Projected Variational Integrators for Degenerate Lagrangian Systems*. 2017.

[38] M. Kraus et al. “GEMPIC: geometric electromagnetic particle-in-cell methods”. In: *Journal of Plasma Physics* 83.4 (2017), p. 905830401.

[39] C. Lubich. “On splitting methods for Schrödinger–Poisson and cubic nonlinear Schrödinger equations”. In: *Mathematics of computation* 77.264 (2008), pp. 2141–2153.

[40] J. E. Marsden and A. Weinstein. “The Hamiltonian structure of the Maxwell–Vlasov equations”. In: *Physica D: nonlinear phenomena* 4.3 (1982), pp. 394–406.

[41] R. I. McLachlan, G. R. W. Quispel, and N. Robidoux. “Geometric integration using discrete gradients”. In: *Philosophical Transactions of the Royal Society of London. Series A: Mathematical, Physical and Engineering Sciences* 357.1754 (1999), pp. 1021–1045.

[42] P. J. Morrison. “Structure and structure-preserving algorithms for plasma physics”. In: *Physics of Plasmas* 24.5 (2017).

[43] P. J. Morrison. “The Maxwell–Vlasov equations as a continuous Hamiltonian system”. In: *Physics Letters A* 80.5-6 (1980), pp. 383–386.

[44] S. Muralikrishnan and R. Speck. “ParaPIF: a parareal approach for parallel-in-time integration of particle-in-Fourier schemes”. In: *arXiv preprint arXiv:2407.00485* (2024).

[45] B. Perse, K. Kormann, and E. Sonnendrücker. “Geometric Particle-in-Cell Simulations of the Vlasov–Maxwell System in Curvilinear Coordinates”. In: *SIAM Journal on Scientific Computing* 43.1 (2021), B194–B218.

- [46] J. Qiang. “Symplectic particle-in-cell model for space-charge beam dynamics simulation”. In: *Physical Review Accelerators and Beams* 21.5 (2018), p. 054201.
- [47] H. Qin et al. “Canonical symplectic particle-in-cell method for long-term large-scale simulations of the Vlasov–Maxwell equations”. In: *Nuclear Fusion* 56.1 (2015), p. 014001.
- [48] G. Quispel and D. I. McLaren. “A new class of energy-preserving numerical integration methods”. In: *Journal of Physics A: Mathematical and Theoretical* 41.4 (2008), p. 045206.
- [49] L. F. Ricketson and J. Hu. “An explicit, energy-conserving particle-in-cell scheme”. In: *Journal of Computational Physics* (2025), p. 114098.
- [50] J. M. Sanz-Serna. “Runge-Kutta schemes for Hamiltonian systems”. In: *BIT Numerical Mathematics* 28.4 (1988), pp. 877–883.
- [51] B. A. Shadwick, A. B. Stamm, and E. G. Evstatiev. “Variational formulation of macro-particle plasma simulation algorithms”. In: *Physics of Plasmas* 21.5 (2014).
- [52] C. N. Shen, A. Cerfon, and S. Muralikrishnan. “A particle-in-Fourier method with semi-discrete energy conservation for non-periodic boundary conditions”. In: *Journal of computational physics* 519 (2024), p. 113390.
- [53] J. Squire, H. Qin, and W. M. Tang. “Geometric integration of the Vlasov–Maxwell system with a variational particle-in-cell scheme”. In: *Physics of Plasmas* 19.8 (2012).
- [54] A. B. Stamm, B. A. Shadwick, and E. G. Evstatiev. “Variational formulation of macroparticle models for electromagnetic plasma simulations”. In: *IEEE Transactions on Plasma Science* 42.6 (2014), pp. 1747–1758.
- [55] J. Villasenor and O. Buneman. “Rigorous charge conservation for local electromagnetic field solvers”. In: *Computer Physics Communications* 69.2-3 (1992), pp. 306–316.
- [56] J. Xiao et al. “Explicit high-order non-canonical symplectic particle-in-cell algorithms for Vlasov–Maxwell systems”. In: *Physics of Plasmas* 22.11 (2015).

A The convergence rate of the high-regularity loop integral approximation

This appendix leverages results found in standard references on spectral and pseudospectral methods [25, 5]. Let $H_{per}^r([0, 1])$ be the Sobolev space of periodic functions on $[0, 1]$ whose first r derivatives are L^2 integrable:

$$H_{per}^r([0, 1]) = \left\{ f \in L^2([0, 1]) : \left(\sum_{k=-\infty}^{\infty} (1 + |k|^{2r}) |\hat{f}_k|^2 \right)^{1/2} < \infty, \text{ where } \hat{f}_k = \int_0^1 f(x) e^{2\pi i k x} dx \right\}. \quad (67)$$

where, for $f \in L^2([0, 1])$, we use the notation $\hat{f} = \mathcal{F}f$, where $\mathcal{F} : L^2([0, 1]) \rightarrow \ell^2$ denotes the Fourier transform. We define

$$\|f\|_{H^r([0,1])} = \left(\sum_{k=-\infty}^{\infty} (1 + |k|^{2r}) |\hat{f}_k|^2 \right)^{1/2}. \quad (68)$$

Note, the boundedness of this Sobolev norm automatically implies periodicity of the function.

For $q, p \in H_{per}^r([0, 1])$, Parseval’s theorem implies that

$$\mathcal{I}(p, q) = \int_0^1 p(s) q'(s) ds = \sum_{k \in \mathbb{Z}} (2\pi i k) \hat{p}_{-k} \hat{q}_k. \quad (69)$$

Hence, we can see that, the loop integral only converges for $p, q \in H_{per}^r([0, 1])$ when $r > 1/2$. Note that the Sobolev embedding theorem implies that $f \in H_{per}^r([0, 1])$ is continuous if $r > 1/2$. Hence, continuity of the data would seem to be a necessary condition for loop integrals to be well-defined in this classical sense.

A.1 The pseudospectral loop integral approximation

We seek an approximation of the loop integral

$$\mathcal{I}(p, q) = \int_0^1 p(s)q'(s)ds \quad (70)$$

using only a finite number of equispaced samples of the phase-space loop. Let $\mathbf{p}_j = p(j/N)$ and $\mathbf{q}_j = q(j/N)$ for $j = 0, \dots, N-1$ be equispaced samples. Let $\tilde{\mathbf{p}}_k$ be the discrete Fourier transform (DFT) of the data:

$$\tilde{\mathbf{f}}_k = \frac{1}{N} \sum_{j=0}^{N-1} \mathbf{p}_j e^{-2\pi i k j / N}, \quad (71)$$

and similarly for $\tilde{\mathbf{q}}_k$. The approximate loop integral takes the form

$$\mathcal{I}_N(p, q) = \sum_{k=0}^{N-1} 2\pi i k \tilde{\mathbf{p}}_{-k} \tilde{\mathbf{q}}_k. \quad (72)$$

Representing the DFT as a matrix, \mathbb{F} , we may write this approximation as

$$\mathcal{I}_N(p, q) = (\mathbb{F} \mathbf{p})^* (2\pi i \text{diag}(\mathbf{k}) \mathbb{F} \mathbf{q}) = \mathbf{p}^T \mathbb{F}^{-1} (2\pi i \text{diag}(\mathbf{k}) \mathbb{F} \mathbf{q}) (1/N). \quad (73)$$

Recalling that $\mathbb{F}^{-1} = N \mathbb{F}^*$ (with the chosen convention for normalizing the DFT), this is approximation scheme is equivalent to an approximation of the loop integral via trapezoidal rule with the derivative of q approximated via a pseudospectral method.

The objective of this section is to establish a tight bound on the error incurred by this approximation:

$$\mathcal{E}(p, q) = |\mathcal{I}(p, q) - \mathcal{I}_N(p, q)|. \quad (74)$$

This is accomplished by finding the error incurred in the two approximation steps:

- We find the truncation error in a Fourier Galerkin approximation of $\mathcal{I}(p, q)$, which assumes access to the exact Fourier coefficients of p and q .
- We approximate the exact Fourier coefficients in terms of the DFT of equispaced data.

The final result follows from finding error bounds on these two approximations.

Lemma 1 (Fourier Galerkin error estimate). *Let $f, g \in H_{per}^r([0, 1])$ for some $r > 1/2$. Define the truncated Fourier series*

$$f_N(x) = \sum_{|k| \leq N} \hat{f}_k e^{2\pi i k x}, \quad g_N(x) = \sum_{|k| \leq N} \hat{g}_k e^{2\pi i k x}, \quad (75)$$

where \hat{f}_k and \hat{g}_k are the Fourier coefficients of f and g , respectively:

$$\hat{f}_k = \int_0^1 f(x) e^{2\pi i k x} dx, \quad \text{and} \quad \hat{g}_k = \int_0^1 g(x) e^{2\pi i k x} dx. \quad (76)$$

Then one finds that

$$\left| \int_0^1 f(x) g'(x) dx - \int_0^1 f_N(x) g'_N(x) dx \right| \leq 2\pi N^{-(2r-1)} \|f\|_{H^r} \|g\|_{H^r}. \quad (77)$$

Proof. We express the integral in terms of Fourier coefficients using Parseval's theorem. The exact integral is

$$\int_0^1 f(x) g'(x) dx = \sum_{k \in \mathbb{Z}} 2\pi i k \hat{f}_{-k} \hat{g}_k. \quad (78)$$

The Galerkin approximation truncates the series at $|k| \leq N$:

$$\int_0^1 f_N(x) g'_N(x) dx = \sum_{|k| \leq N} 2\pi i k \hat{f}_{-k} \hat{g}_k. \quad (79)$$

Thus, the error is the tail:

$$E_N := \left| \sum_{|k| > N} 2\pi i k \hat{f}_{-k} \hat{g}_k \right|. \quad (80)$$

Using the triangle and Cauchy–Schwarz inequalities:

$$\begin{aligned} E_N &\leq 2\pi \sum_{|k| > N} |k|^{-(2r-1)} (|k|^r |\hat{f}_{-k}|) (|k|^r |\hat{g}_k|) \leq 2\pi N^{-(2r-1)} \sum_{|k| > N} (|k|^r |\hat{f}_{-k}|) (|k|^r |\hat{g}_k|) \\ &\leq 2\pi N^{-(2r-1)} \left(\sum_{|k| > N} |k|^{2r} |\hat{f}_{-k}|^2 \right)^{1/2} \left(\sum_{|k| > N} |k|^{2r} |\hat{g}_k|^2 \right)^{1/2} \leq 2\pi N^{-(2r-1)} \|g\|_{H^r} \|f\|_{H^r}. \end{aligned} \quad (81)$$

Because $f, g \in H^r$, we have

$$\sum_{k \in \mathbb{Z}} |k|^{2r} |\hat{f}_k|^2 = \|f\|_{H^r}^2 < \infty, \quad \text{and} \quad \sum_{k \in \mathbb{Z}} |k|^{2r} |\hat{g}_k|^2 = \|g\|_{H^r}^2 < \infty, \quad (82)$$

this bound is valid for $r > 1/2$ for all $f, g \in H_{per}^r([0, 1])$. \square

Next, for completeness, we reproduce a well-known formula relating the discrete Fourier transform (DFT) coefficients with those of the exact Fourier transform. This formula is needed to find the error incurred by approximating the exact Fourier coefficients using the DFT of equispaced data samples.

Lemma 2 (Aliasing formula for DFT approximation of Fourier coefficients). *Let $f \in L^2_{per}([0, 1])$ and define its exact Fourier coefficients by*

$$\hat{f}_k = \int_0^1 f(x) e^{-2\pi i k x} dx. \quad (83)$$

Let $\{f_j\}_{j=0}^{N-1}$ be the samples $f_j = f(j/N)$, and define the DFT by

$$\tilde{f}_k = \frac{1}{N} \sum_{j=0}^{N-1} f_j e^{-2\pi i k j / N}. \quad (84)$$

Then the following aliasing identity holds:

$$\tilde{f}_k = \sum_{\ell \in \mathbb{Z}} \hat{f}_{k+\ell N}. \quad (85)$$

Proof. Express $f(x)$ in its Fourier series:

$$f(x) = \sum_{m \in \mathbb{Z}} \hat{f}_m e^{2\pi i mx}. \quad (86)$$

Insert this into the DFT definition:

$$\tilde{f}_k = \frac{1}{N} \sum_{j=0}^{N-1} \sum_{m \in \mathbb{Z}} \hat{f}_m e^{2\pi i m j / N} e^{-2\pi i k j / N} = \sum_{m \in \mathbb{Z}} \hat{f}_m \cdot \left[\frac{1}{N} \sum_{j=0}^{N-1} e^{2\pi i (m-k) j / N} \right]. \quad (87)$$

The bracketed sum is a periodic Kronecker comb:

$$\frac{1}{N} \sum_{j=0}^{N-1} e^{2\pi i (m-k) j / N} = \begin{cases} 1, & \text{if } m - k \equiv 0 \pmod{N}, \\ 0, & \text{otherwise.} \end{cases} \quad (88)$$

Hence only indices $m = k + \ell N$ survive, yielding

$$\tilde{f}_k = \sum_{\ell \in \mathbb{Z}} \hat{f}_{k+\ell N}, \quad (89)$$

as claimed. \square

Lemma 3 (Fourier coefficient approximation). *Let $f \in H^r_{\text{per}}([0, 1])$ for some $r > 0$, and define its k^{th} Fourier coefficient by*

$$\hat{f}_k = \int_0^1 f(x) e^{-2\pi i k x} dx. \quad (90)$$

Let \tilde{f}_k denote the approximation to \hat{f}_k via the DFT with N equispaced samples:

$$\tilde{f}_k = \frac{1}{N} \sum_{j=0}^{N-1} f\left(\frac{j}{N}\right) e^{-2\pi i k j / N}. \quad (91)$$

Then there exists a constant $C > 0$, independent of k and N , such that for $k < N$,

$$|\tilde{f}_k - \hat{f}_k| \leq C N^{-2r} \|f\|_{H^r([0, 1])}. \quad (92)$$

Proof. From Lemma 2, the DFT coefficient \hat{f}_k , satisfies the aliasing formula:

$$\tilde{f}_k = \sum_{m \in \mathbb{Z}} \hat{f}_{k+mN}. \quad (93)$$

Thus, the error is given by

$$\tilde{f}_k - \hat{f}_k = \sum_{m \in \mathbb{Z} \setminus \{0\}} \hat{f}_{k+mN}. \quad (94)$$

Since $f \in H^r([0, 1])$, its Fourier coefficients satisfy the decay condition

$$|\hat{f}_\ell| \leq C(1 + |\ell|)^{-r} \|f\|_{H^r([0, 1])}. \quad (95)$$

The sum in Equation (94) may be bounded as follows:

$$\sum_{m \neq 0} (1 + |k + mN|^2)^{-r} \leq 2N^{-2r} \sum_{m=1} m^{-2r} = 2\zeta(2r)N^{-2r}, \quad (96)$$

which is finite for $r > 1/2$. \square

Together, these lemmas imply the following theorem establishing the convergence of the Fourier-collocation loop integral approximation.

Theorem 1 (Error in Collocation Approximation). *Let $f, g \in H_{\text{per}}^r([0, 1])$ for some $r > 0$. Let $f_j = f(j/N)$ and $g_j = g(j/N)$ for $j = 0, \dots, N-1$ be equispaced samples. Let \tilde{g}' denote the pseudospectral derivative of g computed using the discrete Fourier transform (DFT) of (g_0, \dots, g_{N-1}) :*

$$\tilde{g}'_j := \sum_{|k| \leq N/2} (2\pi i k) \tilde{g}_k e^{2\pi i k j / N}, \quad \text{where} \quad \tilde{g}_k = \frac{1}{N} \sum_{j=0}^{N-1} g_j e^{-2\pi i k j / N}. \quad (97)$$

Define the discrete approximation to the integral by the trapezoidal rule:

$$\mathcal{I}_N(f, g) := \frac{1}{N} \sum_{j=0}^{N-1} f_j \tilde{g}'_j. \quad (98)$$

Then the total error satisfies

$$\left| \int_0^1 f(x) g'(x) dx - \mathcal{I}_N(f, g) \right| \leq C N^{-(2r-1)} \|f\|_{H^r([0, 1])} \|g\|_{H^r([0, 1])}, \quad (99)$$

for some constant $C > 0$ independent of f, g , and N .

Proof. The proof proceeds by introducing the intermediate Fourier-Galerkin approximation, and bounding the total error using the triangle inequality. Let $\mathcal{I}_N^G(f, g)$ be the Fourier-Galerkin approximation from Lemma 1. Then we have that

$$\left| \int_0^1 f(x) g'(x) dx - \mathcal{I}_N(f, g) \right| \leq \left| \int_0^1 f(x) g'(x) dx - \mathcal{I}_N^G(f, g) \right| + |\mathcal{I}_N^G(f, g) - \mathcal{I}_N(f, g)|. \quad (100)$$

By Lemma 1, we find that

$$\left| \int_0^1 f(x) g'(x) dx - \mathcal{I}_N^G(f, g) \right| \leq 2\pi N^{-(2r-1)} \|f\|_{H^r} \|g\|_{H^r}. \quad (101)$$

Moreover, we find that

$$|\mathcal{I}_N^G(f, g) - \mathcal{I}_N(f, g)| = \left| \sum_{|k| \leq N} 2\pi i k \hat{f}_{-k} \hat{g}_k - \sum_{|k| \leq N} 2\pi i k \tilde{f}_{-k} \tilde{g}_k \right|, \quad (102)$$

where

$$\tilde{f}_k = \frac{1}{N} \sum_{j=0}^{N-1} f_j e^{-2\pi i k j / N}, \quad \text{and} \quad \tilde{g}_k = \frac{1}{N} \sum_{j=0}^{N-1} g_j e^{-2\pi i k j / N}. \quad (103)$$

The triangle inequality and Lemma 3 implies that

$$\begin{aligned} \left| \sum_{|k| \leq N} 2\pi i k \hat{f}_{-k} \hat{g}_k - \sum_{|k| \leq N} 2\pi i k \tilde{f}_{-k} \tilde{g}_k \right| &\leq 2\pi \sum_{|k| \leq N} (|\hat{f}_k - \tilde{f}_k| |\hat{g}_k| + |\tilde{f}_k| |\hat{g}_k - \tilde{g}_k|) \\ &\leq C \sum_{|k| \leq N} (N^{-2r} \|f\|_{H^r} \|g\|_{H^r}) \\ &= CN^{-(2r-1)} \|f\|_{H^r} \|g\|_{H^r}. \end{aligned} \quad (104)$$

The result follows. \square

B The convergence rate of the low-regularity loop integral approximation

The appropriate space to study the convergence of numerical methods for discontinuous functions is the space of functions of bounded variation (BV), whose properties are discussed in standard references on measure theory [18]. The space of functions of bounded variation over the interval $[0, 1]$, $BV([0, 1]) \subseteq L^1([0, 1])$, is defined such that

$$f \in BV([0, 1]) \implies \|f\|_{BV} = \|f\|_{L^1} + TV(f) < \infty, \quad (105)$$

where we define the total variation seminorm to be

$$TV(f) := \sup \left\{ \sum_{i=1}^n |f(x_i) - f(x_{i-1})| : 0 = x_0 < x_1 < \dots < x_n = 1 \right\}, \quad (106)$$

where the supremum is taken over all finite partitions. We define the space of piecewise C^1 functions on the interval $[0, 1]$ to be

$$C_{pw}^1([0, 1]) = \left\{ f \in BV([0, 1]) : \exists N_d \in \mathbb{N}^+, \exists \{s_i\}_{i=0}^{N_d} \subset [0, 1] \text{ such that } s_0 = 0, s_{N_d} = 1, \text{ and } f|_{[s_i, s_{i+1}]} \in C^1([s_i, s_{i+1}]) \right\}. \quad (107)$$

Note, since $C_{pw}^1([0, 1]) \subset BV([0, 1])$, it follows that $f \in C_{pw}^1([0, 1])$ must have a finite number of jump discontinuities. The following lemma allows us to approximate functions of bounded variation by piecewise constant functions.

Lemma 4 (BV approximation error). *Let $f \in BV([a, b])$, and let f_N be a piecewise constant interpolant of f on a uniform grid of N intervals with spacing $\Delta s = 1/N$:*

$$f_N(s) := f(s_i^-) \quad \text{for } s \in [s_i, s_{i+1}). \quad (108)$$

Then

$$\|f - f_N\|_{L^1([0, 1])} \leq \frac{1}{N} \cdot TV(f). \quad (109)$$

Proof. Let $\{s_i = i\Delta s\}_{i=0}^N$ denote the uniform partition of $[0, 1]$, with $\Delta s = 1/N$. On each subinterval $[s_i, s_{i+1})$, we obtain contributions to the L^1 error of the form

$$\int_{s_i}^{s_{i+1}} |f(s) - f(s_i^-)| \, ds. \quad (110)$$

This error is bounded by the total variation of f on that interval times the cell width:

$$\int_{s_i}^{s_{i+1}} |f(s) - f(s_i^-)| \, ds \leq \Delta s \cdot TV_{[s_i, s_{i+1}]}(f). \quad (111)$$

Summing over all cells:

$$\|f - f_N\|_{L^1([0, 1])} = \sum_{i=0}^{N-1} \int_{s_i}^{s_{i+1}} |f(s) - f(s_i^-)| \, ds \leq \Delta s \cdot \sum_{i=0}^{N-1} TV_{[s_i, s_{i+1}]}(f) \leq \Delta s \cdot TV_{[0, 1]}(f). \quad (112)$$

As $\Delta s = 1/N$, we find

$$\|f - f_N\|_{L^1([0, 1])} \leq \frac{1}{N} \cdot TV(f). \quad (113)$$

□

B.1 The piecewise loop integral and its approximation

Consider a parametric loop in phase space, $\gamma : \mathbb{R} \bmod 1 \rightarrow \mathbb{R}^2$ such that $\gamma(s) = (q(s), p(s))$. Suppose that we require $q, p \in C_{pw}^1([0, 1])$. For a given q, p , let $\mathbf{S} = \{s_i\}_{i=1}^{N_d} \subset [0, 1]$ be the collection of discontinuities in either q or p (or both). Hence, q and p are continuously differentiable on the sub-intervals: that is, for $I_i := [s_i, s_{i+1}]$, $q, p \in C^1(I_i)$. Denote this collection of these sub-intervals by \mathcal{S} . We define the loop integral

$$\mathcal{I}(q, p) = \sum_{I_i \in \mathcal{S}} \int_{I_i} p(s) q'(s) ds. \quad (114)$$

That is, the loop integral is defined to be the sum of the integrals of $p dq$ on each smooth sub-interval.

Remark 8. *This is the Lebesgue-Stieltjes integral $\int p dq$ integrated with respect to the part of the radon measure dq which is absolutely continuous with respect to the Lebesgue measure. The reason for excluding the singular part of the measure (the jump discontinuity) in our definition of the loop integral is motivated by the example of the discontinuous symplectic map $\Phi(q, p) = (q + \text{sign}(p), p)$. For the initial loop $\gamma(s) = (\sin(2\pi s), \cos(2\pi s))$, the map simply breaks it into two disjoint pieces. Integrating over the continuous subintervals shows that the loop integral is preserved.*

We seek to approximate this loop integral using only finitely many equispaced samples of γ :

$$(\mathbf{q}_k, \mathbf{p}_k) = \gamma(k\Delta s), \quad \text{for } k \in \{0, 1, \dots, N-1\}, \quad \Delta s := \frac{1}{N}. \quad (115)$$

We assume that $\{k\Delta s\}_{k=0}^{N-1} \cap \mathbf{S} = \emptyset$. This mild assumption is justified since \mathbf{S} is finite and thus has measure zero. Letting $G_i = [i\Delta s, (i+1)\Delta s]$, we define the discrete approximation:

$$\mathcal{I}_N(q, p) := \sum_{\substack{i=0 \\ G_i \cap \mathbf{S} = \emptyset}}^{N-1} \mathbf{p}_i (\mathbf{q}_{i+1} - \mathbf{q}_i). \quad (116)$$

This approximation to the integral is essentially a Riemann sum over each continuous sub-interval, where p is approximated using left-sided piecewise constant shape functions and q by piecewise linear interpolation. The sub-intervals containing discontinuities are omitted. The convergence of this approximation is established in the following theorem.

Theorem 2. *Let $q, p \in C_{pw}^1([0, 1])$, and define $\mathcal{I}(q, p)$ and $\mathcal{I}_N(q, p)$ as in Equations 114 and 116. Then*

$$|\mathcal{I}(q, p) - \mathcal{I}_N(q, p)| \leq \frac{1}{N} (3\|p\|_{L^\infty([0,1])} + TV_{[0,1]}(p)) TV_{[0,1]}(q). \quad (117)$$

Proof. Define

$$p_N(s) = p(s_k), \quad \text{for } s \in [s_k, s_{k+1}], \quad (118)$$

and

$$q_N(s) = \frac{s_{k+1} - s}{\Delta s} q(s_k) + \frac{s - s_k}{\Delta s} q(s_{k+1}), \quad \text{for } s \in [s_k, s_{k+1}]. \quad (119)$$

That is, we approximate p over the sub-interval by a piecewise constant function taking the value of the left endpoint, and q by a piecewise linear polynomial interpolating the grid. Then it follows that

$$\mathcal{I}_N(q, p) = \sum_{\substack{k=0 \\ G_k \cap \mathbf{S} = \emptyset}}^{N-1} \int_{k\Delta s}^{(k+1)\Delta s} p_N(s) q'_N(s) ds. \quad (120)$$

It follows that we can split the error as follows:

$$\begin{aligned} \mathcal{I}(q, p) - \mathcal{I}_N(q, p) &= \sum_{\substack{k=0 \\ G_k \cap \mathbf{s} \neq \emptyset}}^{N-1} \left(\int_{k\Delta s}^{s_k^-} p(s) q'(s) \mathbf{d}s + \int_{s_k^+}^{(k+1)\Delta s} p(s) q'(s) \mathbf{d}s \right) \\ &\quad + \sum_{\substack{k=0 \\ G_k \cap \mathbf{s} = \emptyset}}^{N-1} \int_{G_k} (p(s) q'(s) - p_N(s) q'_N(s)) \mathbf{d}s, \end{aligned} \quad (121)$$

where s_k^\pm simply denotes the left- and right-hand sides of the jump. There are two sources of error: the first term represents the error incurred from omitting the sub-intervals with discontinuities from our quadrature approximation, while the second is the error incurred by quadrature over the continuous sub-intervals.

For each k , we find that

$$\left| \int_{G_k} (p(s) q'(s) - p_N(s) q'_N(s)) \mathbf{d}s \right| \leq \|p - p_N\|_{L^1(G_k)} \|q'\|_{L^\infty(G_k)} + \|q' - q'_N\|_{L^1(G_k)} \|p\|_{L^\infty(G_k)}. \quad (122)$$

We need bound the L^1 error in our approximations of both p and q' . Note that

$$q'_N(s) = \frac{q((k+1)\Delta s) - q(k\Delta s)}{\Delta s}, \quad (123)$$

which is the forward difference approximation of the derivative if evaluated at $s = k\Delta s$. The mean value theorem implies that $\exists s_* \in G_k$ such that

$$|q'(s) - q'_N(s)| = |q'(s) - q'(s_*)| + |q'(s_*) - q'_N(s)| \leq TV_{G_k}(q). \quad (124)$$

Therefore, for $s \in G_k$,

$$|q'(s) - q'_N(s)| \leq |q'(s) - q'(s_*)| + |q'(s_*) - q'_N(s)| \leq TV_{G_k}(q) + TV_{G_k}(q) = 2TV_{G_k}(q). \quad (125)$$

Integrating over G_k , we find that

$$\|q' - q'_N\|_{L^1(G_k)} \leq 2\Delta s TV_{G_k}(q). \quad (126)$$

Likewise, Lemma 4 implies $\|p - p_N\|_{L^1(G_k)} \leq \Delta s TV_{G_k}(p)$. Hence, since $\|q'\|_{L^\infty(G_k)} \leq TV_{G_k}(q)$, we find that

$$\left| \int_{G_k} (p(s) q'(s) - p_N(s) q'_N(s)) \mathbf{d}s \right| \leq \Delta s (TV_{G_k}(p) + 2\|p\|_{L^\infty(G_k)}) TV_{G_k}(q). \quad (127)$$

We further have that

$$\left| \int_{k\Delta s}^{s_k^-} p(s) q'(s) \mathbf{d}s + \int_{s_k^+}^{(k+1)\Delta s} p(s) q'(s) \mathbf{d}s \right| \leq \Delta s \|p\|_{L^\infty(G_k)} TV_{G_k}(q). \quad (128)$$

Hence, summing over all subintervals, we get the bound

$$|\mathcal{I}(q, p) - \mathcal{I}_N(q, p)| \leq \Delta s (3\|p\|_{L^\infty([0,1])} + TV_{[0,1]}(p)) TV_{[0,1]}(q). \quad (129)$$

□

B.2 Detecting jump discontinuities

The discrete loop integral for piecewise continuous loop data requires a priori knowledge of the location of jump discontinuities. We do not generally have access to this. However, we can estimate this set using a grid of equispaced data. Define

$$\mathcal{K}(L_q, L_p) = \left\{ k \in \{0, \dots, N-1\} : \left| \frac{p((k+1)\Delta s) - p(k\Delta s)}{\Delta s} \right| \leq L_p \|p\|_{L^\infty([0,1])} \right. \\ \left. \text{and } \left| \frac{q((k+1)\Delta s) - q(k\Delta s)}{\Delta s} \right| \leq L_q \|q\|_{L^\infty([0,1])} \right\}, \quad (130)$$

where $L_q, L_p > 0$ are user-supplied constants acting as cutoffs for the maximum allowed value for the derivative normalized by the infinity norm. Then the approximate piecewise smooth loop integral may be computed as

$$\mathcal{I}_N(q, p; L_q, L_p) = \sum_{k \in \mathcal{K}(L_q, L_p)} p_k (q_{k+1} - q_k). \quad (131)$$

Empirically, we have found that letting $L_q = L_p = 10^3$ is adequate for the problems considered in this work, but some experimentation may be needed in general. These parameters should be set large enough that large derivatives (which are not true discontinuities) are not spuriously removed. Note, the approximation will only begin to converge for $N > \max(L_q, L_p)$.

C On the regularity of B-splines in 1D

Consider the constant cardinal B-spline,

$$B_0(x) = \begin{cases} 1, & |x| \leq 1 \\ 0, & \text{else.} \end{cases} \quad (132)$$

Its Fourier transform is

$$\hat{B}_0(k) = \frac{1}{\sqrt{2\pi}} \text{sinc}\left(\frac{k}{2}\right). \quad (133)$$

It is possible to show that

$$\int_{\mathbb{R}} (1+k^2)^s |\hat{B}_0(k)|^2 dk < \infty \quad (134)$$

for $s \in [0, 1/2)$, since $\text{sinc}(k) \sim 1/k$ as $|k| \rightarrow \infty$. The degree- p cardinal B-spline is

$$B_p = \underbrace{(B_0 * B_0 * \dots * B_0)}_{p+1 \text{ times}}(x). \quad (135)$$

Proceeding similarly to the case of linear B-splines, we find that

$$\hat{B}_p(k) = \left[\frac{1}{\sqrt{2\pi}} \text{sinc}\left(\frac{k}{2}\right) \right]^{p+1}, \quad (136)$$

and therefore, we conclude that

$$\int_{\mathbb{R}} (1+k^2)^s |\hat{B}_p(k)|^2 dk < \infty, \quad (137)$$

for $s \in [0, p + 1/2)$, since

$$(1 + k^2)^s |\hat{B}_p(k)|^2 \sim \frac{1}{k^{2(p+1-s)}} \quad \text{as } k \rightarrow \infty. \quad (138)$$

Thus, it follows that $B_p \in H^{p+1/2-\epsilon}(\mathbb{R})$ for all $\epsilon > 0$. Because $H^s(\mathbb{R})$ is closed under scaling, translation, and (countable) addition, it follows that the span of general compactly supported degree- p B-splines are likewise in $H^{p+1/2-\epsilon}(\mathbb{R})$. This includes all compactly supported functions on \mathbb{R} which have been interpolated in a B-spline basis.

D On the symplecticity of Strang splitting

As the numerical tests in this work utilize Strang splitting for their time-stepping, and we operate under the assumption that this time-advance map is symplectic, it is helpful to briefly demonstrate the symplecticity of the method to keep this work self-contained. The symplecticity of this method is well-known and may be demonstrated by several different approaches [27], e.g. by deriving the method via Hamiltonian splitting, as a variational integrator, or as a symplectic partitioned Runge-Kutta method [50].

Consider a Lagrangian system of the form

$$L(\mathbf{q}, \dot{\mathbf{q}}) = \frac{1}{2} |\dot{\mathbf{q}}|^2 - V(\mathbf{q}). \quad (139)$$

The conjugate momentum is given by $\mathbf{p} = \partial L / \partial \dot{\mathbf{q}} = \dot{\mathbf{q}}$. The type-I generating function mapping $\mathbf{q}_0 = \mathbf{q}(t_0)$ to $\mathbf{q}_1 = \mathbf{q}(t_1)$ is given by Hamilton's principle function:

$$S_1(\mathbf{q}_0, \mathbf{q}_1; t_0, t_1) = \int_{t_0}^{t_1} \left(\frac{1}{2} |\dot{\mathbf{q}}|^2 - V(\mathbf{q}) \right) dt. \quad (140)$$

The symplectic map from $(\mathbf{q}_0, \mathbf{p}_0)$ to $(\mathbf{q}_1, \mathbf{p}_1)$ is implicitly defined by the system

$$\partial_{\mathbf{q}_0} S_1(\mathbf{q}_0, \mathbf{q}_1; t_0, t_1) = -\mathbf{p}_0, \quad \text{and} \quad \partial_{\mathbf{q}_1} S_1(\mathbf{q}_0, \mathbf{q}_1; t_0, t_1) = \mathbf{p}_1. \quad (141)$$

Suppose we approximate the generating function using trapezoidal rule with the time derivative approximated by forward and backward differences at the endpoints $t = t_0$ and $t = t_1$, respectively. This yields the generating function

$$S_d(\mathbf{q}_0, \mathbf{q}_1, t_0, t_1) = \frac{h}{2} \left(\left| \frac{\mathbf{q}_1 - \mathbf{q}_0}{h} \right|^2 - V(\mathbf{q}_0) - V(\mathbf{q}_1) \right). \quad (142)$$

The symplectic map implied by equation (141) may be solved explicitly yielding

$$\begin{aligned} \mathbf{q}_1 &= \mathbf{q}_0 + h \left(\mathbf{p}_0 - \frac{h}{2} \nabla V(\mathbf{q}_0) \right) \\ \mathbf{p}_1 &= \mathbf{p}_0 - \frac{h}{2} \left[\nabla V(\mathbf{q}_0) + \nabla V \left(\mathbf{q}_0 + h \left(\mathbf{p}_0 - \frac{h}{2} \nabla V(\mathbf{q}_0) \right) \right) \right], \end{aligned} \quad (143)$$

which may be alternatively written as

$$\begin{aligned} \mathbf{p}_{1/2} &= \mathbf{p}_0 - \frac{h}{2} \nabla V(\mathbf{q}_0) \\ \mathbf{q}_1 &= \mathbf{q}_0 + h \mathbf{p}_{1/2} \\ \mathbf{p}_1 &= \mathbf{p}_{1/2} - \frac{h}{2} \nabla V(\mathbf{q}_1). \end{aligned} \quad (144)$$

This is the *momentum first* Strang splitting method. This derivation as a variational integrator is instructive, but unfortunately the corresponding *position first* version of the algorithm does not admit a similarly simple and intuitive derivation.

However, we can derive both forms of Strang splitting as symplectic partitioned Runge-Kutta methods, which may be shown to be variational integrators in general [27]. Consider a differential equation of the form

$$\dot{\mathbf{q}} = \mathbf{f}(\mathbf{q}, \mathbf{p}), \quad \dot{\mathbf{p}} = \mathbf{g}(\mathbf{q}, \mathbf{p}). \quad (145)$$

If (a_{ij}, b_i) and $(\hat{a}_{ij}, \hat{b}_i)$ are the Butcher tableau for two Runge-Kutta methods, a partitioned Runge-Kutta method for the system is specified by the system:

$$\begin{aligned} \mathbf{k}_i &= \mathbf{f} \left(\mathbf{q}_0 + h \sum_{j=1}^s a_{ij} \mathbf{k}_j, \mathbf{p}_0 + h \sum_{j=1}^s \hat{a}_{ij} \ell_j \right), \\ \ell_i &= \mathbf{g} \left(\mathbf{q}_0 + h \sum_{j=1}^s a_{ij} \mathbf{k}_j, \mathbf{p}_0 + h \sum_{j=1}^s \hat{a}_{ij} \ell_j \right), \\ \mathbf{q}_1 &= \mathbf{q}_0 + h \sum_{i=1}^s b_i \mathbf{k}_i, \quad \mathbf{p}_1 = \mathbf{p}_0 + h \sum_{i=1}^s \hat{b}_i \ell_i. \end{aligned} \quad (146)$$

We can approximate a canonical Hamiltonian system with Hamiltonian $\mathcal{H}(\mathbf{q}, \mathbf{p})$ by letting

$$\mathbf{f}(\mathbf{q}, \mathbf{p}) = \nabla_{\mathbf{q}} \mathcal{H}(\mathbf{q}, \mathbf{p}), \quad \text{and} \quad \mathbf{g}(\mathbf{q}, \mathbf{p}) = -\nabla_{\mathbf{p}} \mathcal{H}(\mathbf{q}, \mathbf{p}). \quad (147)$$

In this case, the map $(\mathbf{q}_0, \mathbf{p}_0) \mapsto (\mathbf{q}_1, \mathbf{p}_1)$ is symplectic if $b_i \hat{a}_{ij} + \hat{b}_j a_{ji} = b_i \hat{b}_j$ [27, 50]. Further, if the Hamiltonian is additively separable, that is if $\mathcal{H}(\mathbf{q}, \mathbf{p}) = T(\mathbf{p}) + V(\mathbf{q})$, the condition $b_i = \hat{b}_i$ is no longer needed to ensure symplecticity.

Now, consider a separable Hamiltonian $\mathcal{H}(\mathbf{q}, \mathbf{p}) = \frac{1}{2} |\mathbf{p}|^2 + V(\mathbf{q})$, yielding:

$$\dot{\mathbf{q}} = \mathbf{p}, \quad \dot{\mathbf{p}} = -\nabla V(\mathbf{q}). \quad (148)$$

As we previously saw, the momentum-first Strang splitting scheme is:

$$\begin{aligned} \mathbf{p}_{1/2} &= \mathbf{p}_0 - \frac{h}{2} \nabla V(\mathbf{q}_0), \\ \mathbf{q}_1 &= \mathbf{q}_0 + h \mathbf{p}_{1/2}, \\ \mathbf{p}_1 &= \mathbf{p}_{1/2} - \frac{h}{2} \nabla V(\mathbf{q}_1). \end{aligned}$$

This scheme has the Butcher tableau:

$$\begin{array}{c|cc} a & 0 & 0 \\ \hline b & 1 & 0 \\ & 1 & 0 \end{array} \quad \text{and} \quad \begin{array}{c|cc} \hat{a} & \frac{1}{2} & 0 \\ \hline \hat{b} & \frac{1}{2} & 0 \\ & \frac{1}{2} & \frac{1}{2} \end{array} \quad (149)$$

Symplecticity holds: $b_1 \hat{a}_{11} + \hat{b}_1 a_{11} = b_1 \hat{a}_{12} + \hat{b}_2 a_{21} = 1/2 = b_1 \hat{b}_1 = b_1 \hat{b}_2$ (the other terms vanish). On the other hand, the position-first Strang splitting scheme is:

$$\begin{aligned} \mathbf{q}_{1/2} &= \mathbf{q}_0 + \frac{h}{2} \mathbf{p}_0, \\ \mathbf{p}_1 &= \mathbf{p}_0 - h \nabla V(\mathbf{q}_{1/2}), \\ \mathbf{q}_1 &= \mathbf{q}_{1/2} + \frac{h}{2} \mathbf{p}_1. \end{aligned}$$

This scheme has the Butcher tableau:

$$\frac{a}{b} = \begin{array}{|c|c|} \hline \frac{1}{2} & 0 \\ \hline \frac{1}{2} & 0 \\ \hline \frac{1}{2} & \frac{1}{2} \\ \hline \end{array}, \quad \text{and} \quad \frac{\hat{a}}{\hat{b}} = \begin{array}{|c|c|} \hline 0 & 0 \\ \hline 1 & 0 \\ \hline 0 & 1 \\ \hline \end{array}. \quad (150)$$

As with the prior case, the symplecticity condition is satisfied.

E Two-cell, single-particle linear PIC evolution equations

We wish to demonstrate that it is possible to obtain a single particle in an absolute value potential as a special case of the linear PIC method described in section 5.1. This can arise in the minimal example of a single particle influenced by its own field in a domain with only two cells. Let the domain $\Omega = [-L, L]$ be divided into two cells: $\Omega_- = [-L, 0]$ and $\Omega_+ = [0, L]$ and identify the endpoints. The grid has only two nodes, $x_0 = 0$ and $x_L = \pm L$. Hence, there are only two shape functions:

$$B_0(x) = 1 - \left| \frac{x}{L} \right|, \quad \text{and} \quad B_L(x) = \left| \frac{x}{L} \right|. \quad (151)$$

The discrete Laplacian associated with this basis is

$$\mathbb{L} = \frac{2}{L} \begin{bmatrix} 1 & -1 \\ -1 & 1 \end{bmatrix}. \quad (152)$$

We now wish to discern the evolution equation for a single particle (x_p, v_p) influenced by its own potential interpolated to this grid. The values of the potential at the two grid-points are therefore found to be

$$\frac{1}{\Delta x} \begin{bmatrix} 1 & -1 \\ -1 & 1 \end{bmatrix} \begin{bmatrix} \phi_0 \\ \phi_L \end{bmatrix} = \frac{1}{L} \begin{bmatrix} 1/2 - B_0(x_p) \\ 1/2 - B_L(x_p) \end{bmatrix}, \quad (153)$$

where we let $\rho_0 = 1/(2L)$ and $w_a = 1/L$ to achieve overall charge neutrality. Before proceeding, note that

$$E_h(x) = -\frac{d\phi_h}{dx} = -(\phi_0 B'_0(x) - \phi_L B'_L(x)) = (\phi_0 - \phi_L) B'_L(x) = (\phi_0 - \phi_L) \text{sign}(x), \quad (154)$$

since

$$B'_0(x) = -B'_L(x) = -\frac{1}{L} \text{sign}(x). \quad (155)$$

Finally, note that

$$\phi_0 - \phi_L = \frac{1}{2} \left(\frac{1}{2} - B_0(x_p) \right) = \frac{1}{2} \left(-\frac{1}{2} + \left| \frac{x_p}{L} \right| \right). \quad (156)$$

Therefore, the evolution equations are given by

$$\dot{x}_p = v_p, \quad \dot{v}_p = \frac{1}{2L} \left(-\frac{1}{2} + \left| \frac{x_p}{L} \right| \right) \text{sign}(x_p). \quad (157)$$

These are just Hamilton's equations generated by the Hamiltonian

$$\mathcal{H}(x_p, v_p) = \frac{v_p^2}{2} + \frac{1}{4} \left(\left| \frac{x_p}{L} \right| - \frac{x_p^2}{L^2} \right). \quad (158)$$

For $x_p \ll L$, we recover trajectories which resemble those from the absolute value potential.